

Chapter 2

**Experimental details and theoretical
concepts**

This chapter deals with materials and methodologies employed in synthesizing conducting polymer poly (3, 4-ethylene-dioxythiophene) polystyrene sulfonic acid (PEDOT-PSS) and their respective nanocomposites with 2D materials like graphene oxide (GO) and tungsten disulfide (WS_2) and metal nanoparticles (AuNP). The synthesis procedure for another conducting polymer, Polyaniline (PANI) and its matrix with Polyvinyl alcohol (PVA) is also described. The physical properties of all the materials and reagents have been thoroughly explained. This chapter also presents the detailing of how conducting polymer-based nanocomposites can be functionalized with biomolecules (Antibody/Enzyme). It also explains the principles of various characterization techniques that are used to study different properties of PEDOT-PSS and PANI based nanocomposites. The theories behind different electrochemical techniques that have been used during the experiments are also described.

2.1. Parent materials

3,4-ethylenedioxythiophene ($EDOT \geq 97\%$) and polystyrene sulfonate (PSS) are procured from Sigma Aldrich[®], which serve as a key component during the synthesis of parent conducting polymer PEDOT-PSS. The oxidizing agent Lithium Perchlorate ($LiClO_4$, 95+%) used during the polymerization of EDOT and solvent acetonitrile (95%) used during the synthesis of PEDOT-PSS were also received from Sigma Aldrich[®]. The indium tin oxide (ITO) coated glass substrate for deposition of synthesized material was obtained from Macwin India[®] Pvt. Ltd.

For the functionalization of conducting polymer matrix, 2D material, like GO and WS_2 were synthesized. For the preparation of graphene oxide, Graphite fine powder (Purity 98%), and oxidizing agent, potassium permanganate ($KMnO_4 \geq 98.5\%$), sodium nitrate ($NaNO_3 \geq 99\%$) all were procured from Sigma Aldrich[®]. On the other hand, for the synthesis of WS_2 nanosheets, bulk WS_2 powder (WS_2 , 99%), solvent N- Methyl-2-pyrrolidone (NMP, 99.5%) were purchased from the same source.

The gold nanoparticles used to decorate the 2D material/PEDOT-PSS based electrode surface which were prepared by reducing Gold (III) chloride hydrate ($HAuCl_4 \cdot H_2O$, 99.9%) in presence of potassium chloride ($KCl \geq 98.5\%$) solution, both were procured from Sigma Aldrich[®].

The monomer aniline, (99%) which is required for the synthesis of PANI was procured from Merck Life Science[®] Pvt. Ltd, Germany. The oxidants, Ammonium peroxydisulfate ($\geq 98\%$) and sodium nitrate ($\geq 99\%$), were also sourced from Merck Life Science[®] Pvt. Ltd, while hydrochloric acid (36%) was obtained from Sigma Aldrich[®].

Glutaraldehyde used for activation of functional groups during immobilization of antibody/enzyme was received from Merck Life Science[®] Pvt. Ltd. Bovine serum albumin (BSA) used as a blocking agent was procured from Sigma Aldrich[®]. Potassium ferricyanide and phosphate buffer saline were procured from Sigma Aldrich[®].

The monoclonal anti-Aflatoxin B₁, human serum IgG and mouse IgG have been procured from Sigma Aldrich[®]. AF-B₁ is procured from MedChem Express, United States. Enzyme glucose oxidase and analyte D-glucose along with ascorbic acid, sucrose and uric acid used for selectivity test all were purchased from SRL chemicals[®] Ltd.

Physical properties of the various materials and reagents used during the work is shown in the following tables.

Table 2.1: Physical properties of monomer.

Materials used	Molecular formula	Molecular weight (g/mol)	Boiling point (°C)	Density (g/cm ³)	Melting point (°C)
EDOT	C ₆ H ₆ O ₂ S	142.18	193	1.331	10-11
Aniline	C ₆ H ₅ NH ₂	93.13	184.1	1.02	-6.3

Table 2.2: Physical properties of functionalizing agents.

Materials used	Molecular formula	Molecular weight (g/mol)	Boiling point ($^{\circ}\text{C}$)	Density (g/cm^3)	Melting point ($^{\circ}\text{C}$)
PSS	$(\text{C}_8\text{H}_7\text{NaO}_3\text{S})_n$	~70000	-	4.35	460
Graphene oxide	$\text{C}_x\text{H}_y\text{O}_z$	364.45	-	0.981	-
Tungsten disulfide	WS_2	247.98	-	7.5	1250
Gold (III) chloride hydrate	$\text{HAuCl}_4 \cdot 3\text{H}_2\text{O}$	339.79	298	3.9	254
Polyvinyl Alcohol	$(\text{C}_2\text{H}_4\text{O})_n$	115000	228	1.19-1.31	200

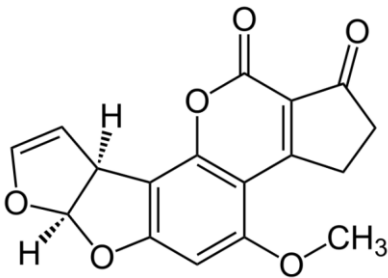
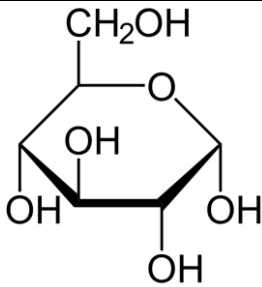
Table 2.3: Physical properties of oxidizing agents and solvents.

Materials used	Molecular formula	Molecular weight (g/mol)	Boiling point ($^{\circ}\text{C}$)	Density (g/cm^3)	Melting point ($^{\circ}\text{C}$)
Lithium perchlorate	LiClO_4	106.39	430	2.42	236
Acetonitrile	CH_3CN	41.05	82	0.78	-45
Sulfuric acid	H_2SO_4	98.079	337	1.83	10.31
Sodium nitrate	NaNO_3	84.9947	380	2.26	308
Potassium permanganate	KMnO_4	158.034	100	2.7	240
NMP	$\text{C}_5\text{H}_9\text{NO}$	99.133	202	1.03	-24
Ammonium peroxydisulfate	$(\text{NH}_4)_2\text{S}_2\text{O}_8$	228.20	-	1.98	120

Table 2.4: Physical properties of the biofunctionalization element, blocking agent and enzyme.

Materials used	Molecular formula	Molecular weight (g/mol)	Boiling point ($^{\circ}\text{C}$)	Density (g/cm^3)	Melting point ($^{\circ}\text{C}$)
Glutaraldehyde	$\text{C}_5\text{H}_8\text{O}_2$	100.12	187	1.06	-14
Bovine serum albumin	$\text{C}_8\text{H}_{21}\text{NOSi}_2$	66430		3.5-5	63
Glucose Oxidase	$(\text{C}_6\text{H}_{10}\text{O}_5)_n$	160		1.0	

Table 2.5: Physical properties of the analytes.

Materials used	Molecular formula	Molecular weight (g/mol)	Molecular structure
Aflatoxin B ₁	$\text{C}_{17}\text{H}_{12}\text{O}_6$	312.277	
Glucose	$\text{C}_6\text{H}_{12}\text{O}_6$	180.156	

2.2. Synthesis steps and optimization-system I (Au/GO/PEDOT-PSS)

2.2.1. PEDOT-PSS over ITO electrode

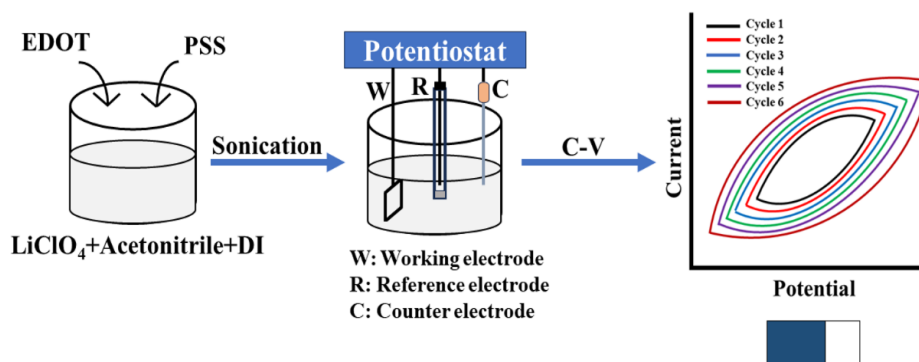


Figure 2.1: Schematic illustration for the preparation of PEDOT-PSS/ITO electrode.

For the preparation of PEDOT-PSS based film over ITO electrode, an electrochemical method has been employed [1]. Prior to all, a monomer solution was prepared by taking 0.1 M EDOT, 0.05 M lithium perchlorate and 5% (w/w) PSS. All were added to acetonitrile+DI water in 3:2 ratio followed by 30 minutes of ultrasonication. The schematic illustration for the synthesis of PEDOT-PSS is shown in Figure 2.1. Electropolymerization technique has been adopted to process PEDOT-PSS over ITO electrode by running cyclic voltammetry (CV) within a potential window -0.2 V - 1.2 V [2]. The deposition curves for the synthesis of PEDOT-PSS over ITO can be found in Figure 2.2. The potential was cycled 6 times at a scan rate of 20 mV/s vs. Ag/AgCl as shown in the Figure.

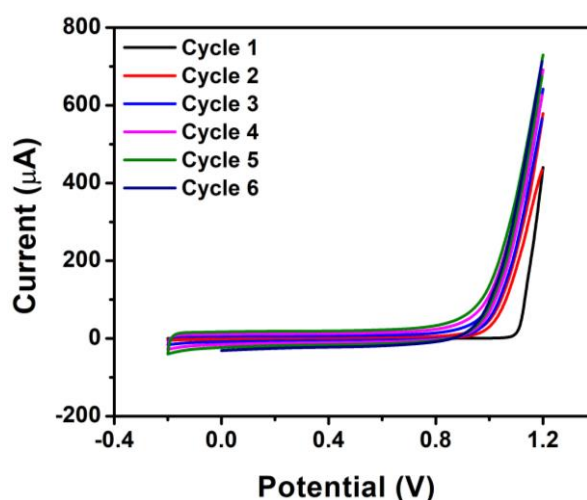


Figure 2.2: Deposition curve of PEDOT-PSS film on ITO at a scan rate of 20 mV/s.

2.2.2. 2D material (Graphene oxide)

Graphene oxide (GO) was synthesized by following the procedure of modified Hummer's method [3]. The schematic illustration for synthesis of GO is shown in Figure 2.3. At first 3 g graphite powder was added to 100 mL of sulphuric acid, then the solution was kept at constant stirring for a few minutes and 1.5 g of NaNO_3 was added simultaneously. Subsequently the mixture was taken in an ice bath to keep the temperature below 20°C and then slowly KMnO_4 (9 g) was added to the mixture keeping temperature below 20°C with the help of ice bath under vigorous stirring. The bath was removed and brought the suspension to $27^\circ\text{C} \pm 3^\circ\text{C}$ and kept for 30 min under stirring. After successful reaction, the colour of the solution became dark brown-green and then 140 mL of DI water was added drop wise with constant evolution of brown fumes and the solution was kept at 95°C for 10 min. To remove unreacted KMnO_4 , 20 mL H_2O_2 was added to the solution and it became brown and then 420 mL of DI water was further added to the mixture to eliminate excess of KMnO_4 . HCl and DI water was added in 3:1 ratio and centrifuged at 5,000 rpm for 7 min to separate liquid from solid / to remove the supernatant. The remaining residuals were rewashed again with HCl and DI water. The washed graphene oxide product was dried at room temperature for 24 h to yield the desired GO powder.

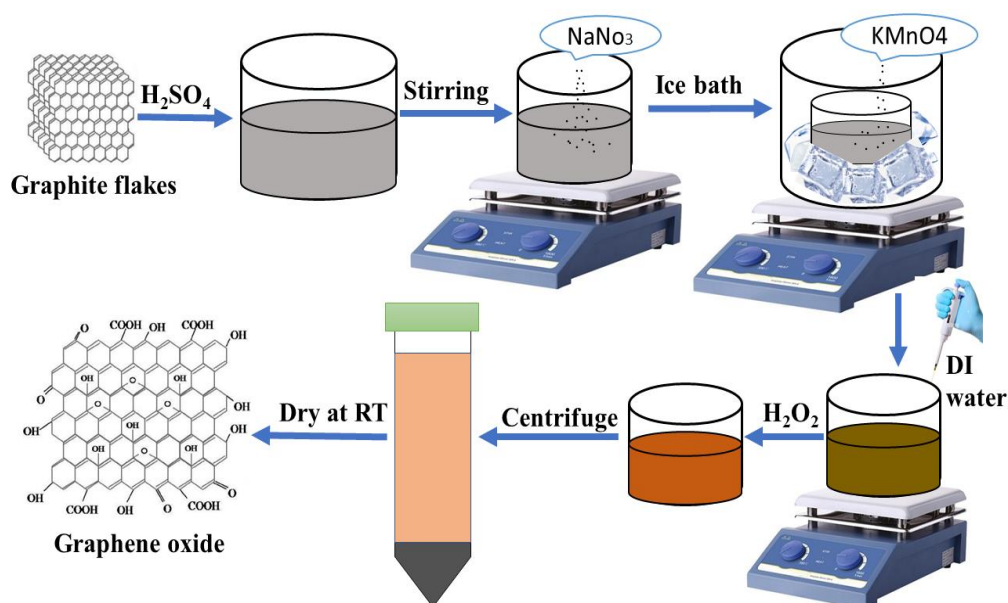


Figure 2.3: Schematic illustration for synthesis of graphene oxide.

2.2.3 GO/PEDOT-PSS over ITO electrode

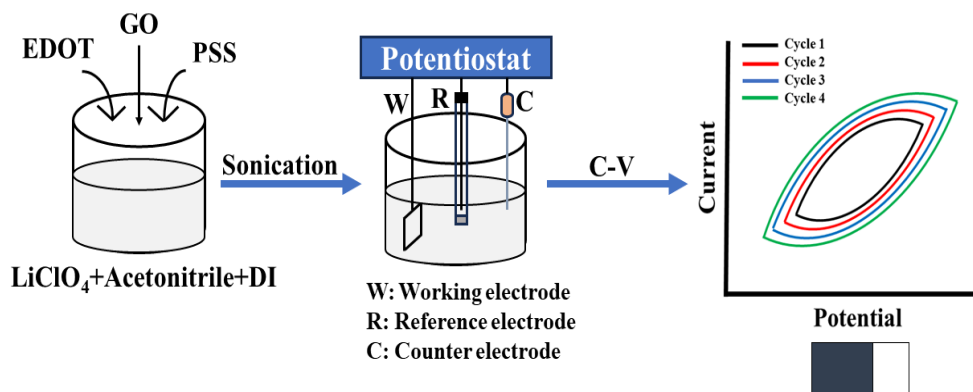


Figure 2.4: Schematic illustration for preparation of GO/PEDOT-PSS/ITO electrode.

PEDOT-PSS modified GO over ITO was prepared by electro-polymerization of monomer EDOT by keeping 10 mg/mL of GO (50 μL) as dopant [4,5]. A schematic illustration of the synthesis of the GO/PEDOT-PSS electrode can be found in Figure 2.4. The electrolyte was prepared by taking 0.1 M EDOT with lithium perchlorate (0.05 M) and 5% (w/w) PSS. Deionized (DI) water and acetonitrile were added to the precursor in 2:3 ratio and subjected to ultrasonication for about 25 min. Electro polymerization was carried out using CV by taking a potential window from -0.2 V to 1.2 V [6]. The potential was cycled for 4 times at a scan rate of 20 mV/sec vs Ag/AgCl and the resulted deposition curve is shown in Figure 2.5.

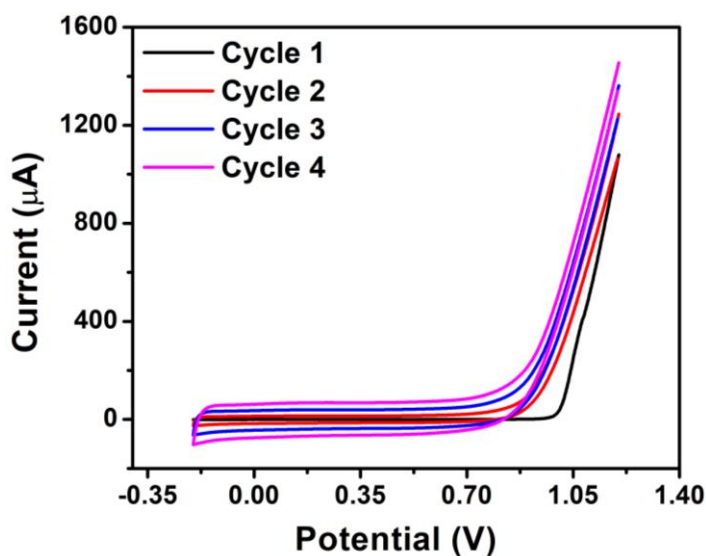


Figure 2.5: Deposition curve of GO/PEDOT-PSS film on ITO at a scan rate of 20 mV/s.

2.2.4. AuNPs over GO/PEDOT-PSS/ITO electrode

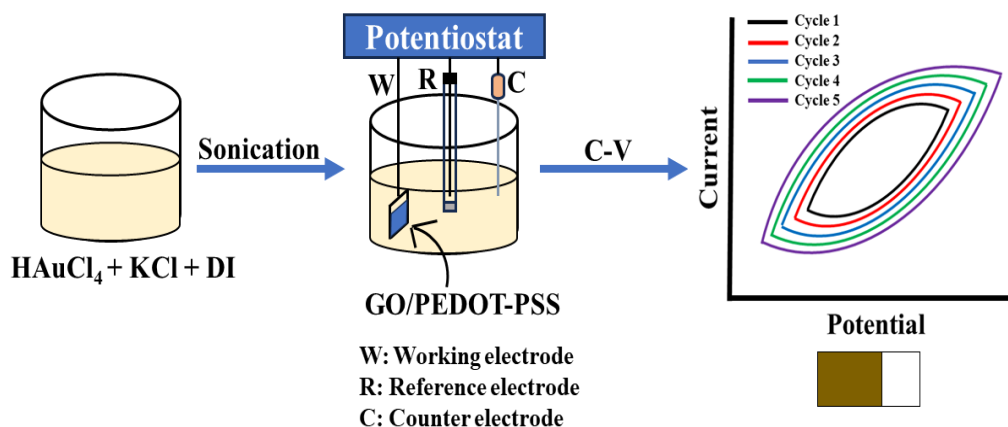


Figure 2.6: Schematic illustration of preparation of Au/GO/PEDOT-PSS/ITO electrode.

The AuNP layers were deposited on the GO/PEDOT-PSS composite film by reducing auric acid through the application of a reduction potential using cyclic voltammetry. The schematic for preparation of AuNP/GO/PEDOT-PSS based electrode is shown in Figure 2.6. Initially, synthesized GO functionalized PEDOT-PSS/ITO electrode was dipped into a 0.1 M KCl solution in presence of 0.5 mL of 3 mM HAuCl_4 stock solution. Then CV was carried out at a scan rate of 20 mV/s within the potential -0.2 V - 1.2 V to obtain AuNP/GO/PEDOT-PSS electrode [7]. CV was carried out for 5 cycles, shown in Figure 2.7. After each cycle, the area under the CV curves increases and indicating adequate deposition of AuNPs over the GO functionalized PEDOT-PSS electrode. Due to the presence of the AuCl_4^- and AuCl_2^- ions over the surface of the nanoparticles their surfaces are negatively charged and are uniformly distributed over the GO/PEDOT-PSS/ITO electrode surface. Notably, the number of layers has been varied from 1st to 7th and corresponding CV was recorded. The CV responses of AuNP/GO/PEDOT-PSS electrodes were taken in 0.1 M PBS by varying the AuNP deposition cycle. The current response is comparatively found to be low in the oxidation region for 1 and 2 cycles of Au deposition. As gold deposition cycles get increased, the current response increases which may be due to the increase in AuNP over the surface that are oxidative at that potential.

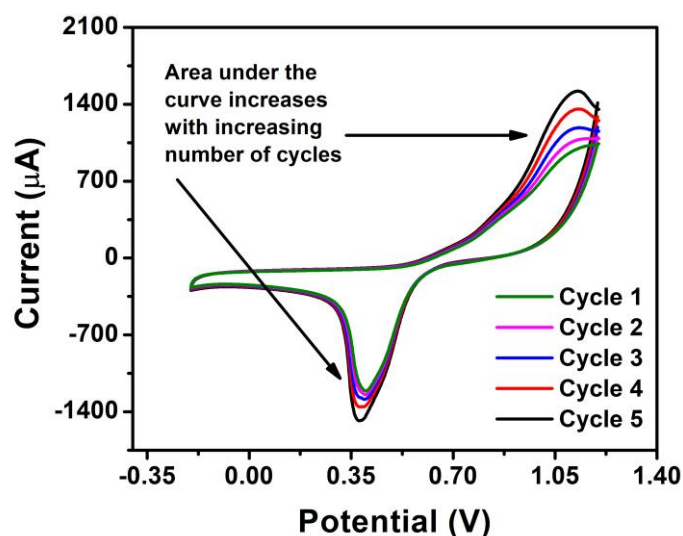


Figure 2.7: Deposition curves of AuNP/GO/PEDOT-PSS films on ITO at a scan rate of 20 mV/s.

Another thing can be noted that the AuNP reduction peak height at ~ 0.4 V increases with increasing the number of AuNP deposition cycles.

With an increased number of layers of Au deposition, beyond 5 layers of Au deposition, the film started peeling off after further procedures, so we decided to use 5 layers of deposition as the optimized one.

2.3. Synthesis steps and optimization-system II (Au/WS₂/PEDOT-PSS)

2.3.1. 2D material (WS₂ nanosheets)

WS₂ nanosheets were synthesized by employing the exfoliation technique suggested by Coleman et al. [8]. The schematic for the preparation of WS₂ nanosheets is shown in Figure 2.8. Initially, 1 mg mL⁻¹ of bulk WS₂ was dispersed in N-methyl-2-pyrrolidone (NMP), which was then put in a bath sonicator (Frequency: 50 Hz power: 100 W) for five hours. In the course of the sonication, the solution was shaken every ten minutes in order to ensure a good result of exfoliation. Thereafter, centrifugation was carried out at 3500 RPM (rotation per minute), for 15 minutes, to separate the product from supernatant. After performing centrifugation, the WS₂ sheets settled on the walls and bottom of the centrifuge tubes. After the precipitate was obtained, they were washed in order to remove any contaminants. Finally, the final wet precipitates were dried at 60 °C for a period of 12 h so that the nanosheets could be formed.

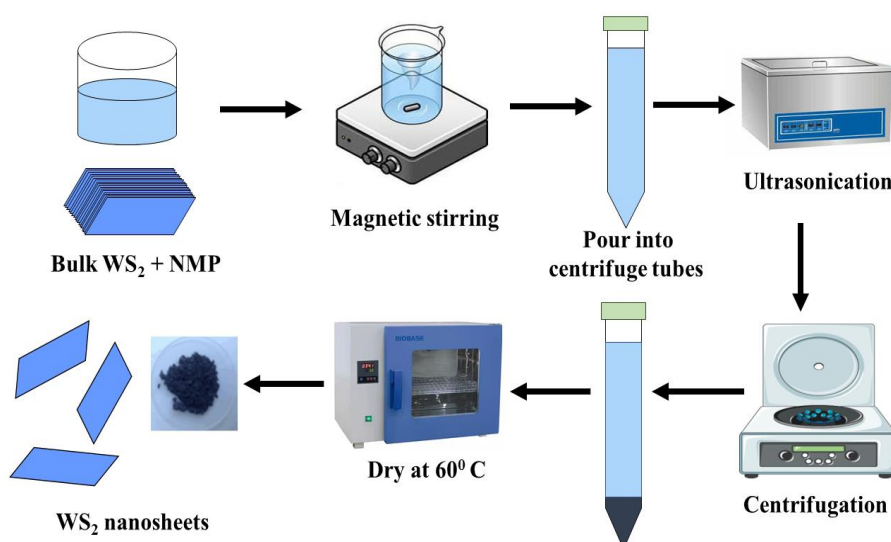


Figure 2.8: Schematic illustration of synthesis of WS₂ nanosheets.

2.3.2. WS₂/PEDOT-PSS over ITO electrode

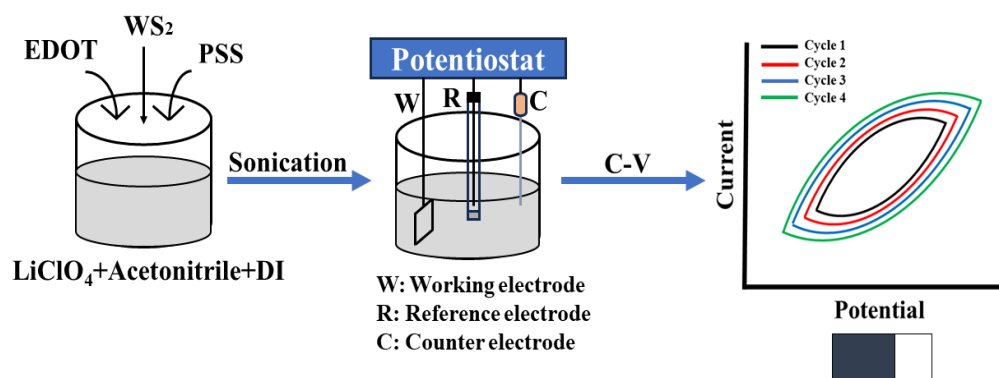


Figure 2.9: Schematic illustration of preparation of WS₂/PEDOT-PSS/ITO electrode.

In order to develop WS₂/PEDOT-PSS/ITO electrode, electro- polymerization of the EDOT monomer was carried out in presence of PSS by taking WS₂ as a dopant. One scheme to show the synthesis of WS₂/PEDOT-PSS/ITO electrode is depicted in Figure 2.9. In the presence of 50 μL of WS₂ and 5% (w/w) PSS, 0.05 M LiClO₄ was added to 0.1 M EDOT with a solution of acetonitrile and DI water in a ratio of 3:2. Afterwards, sonication was performed for 30 minutes to get a homogeneous solution. Finally, Cyclic Voltammetry was carried out for 4 cycles in a potential window from -0.2 V to 1.2 V with a scan rate of 20 mV/s [9]. The deposition CV curve for WS₂/PEDOT-PSS/ITO electrode is shown in Figure 2.10.

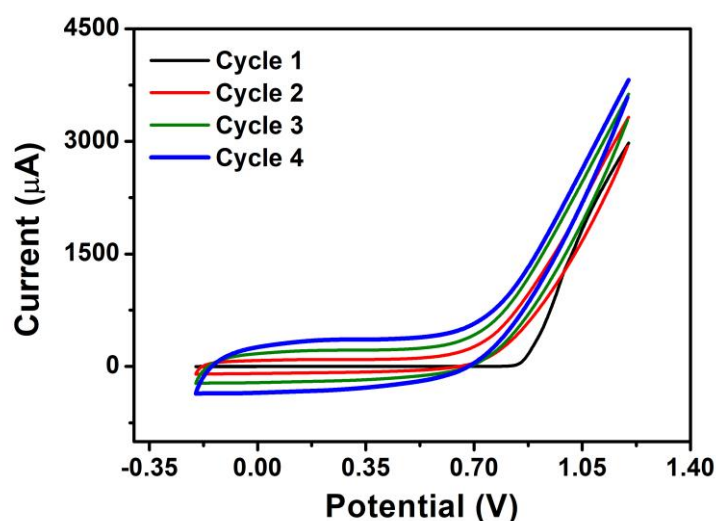


Figure 2.10: Deposition curves of $\text{WS}_2/\text{PEDOT-PSS}/\text{ITO}$ electrode within the potential window from -0.2 V to 1.2 V.

2.3.3. AuNPs on to $\text{WS}_2/\text{PEDOT-PSS}/\text{ITO}$ electrode

The layers of AuNP were deposited on the surface of WS_2 incorporating PEDOT-PSS composite film by reducing auric acid using cyclic voltammetry. The schematic illustration for the preparation of $\text{Au}/\text{WS}_2/\text{PEDOT-PSS}/\text{ITO}$ electrode is shown in Figure 2.11. As an initial step, the synthesized $\text{WS}_2/\text{PEDOT-PSS}/\text{ITO}$ electrode was dipped in a vial containing a solution of 0.1 M KCl followed by addition of 3 mM HAuCl_4 with an amount of 0.5 mL [10].

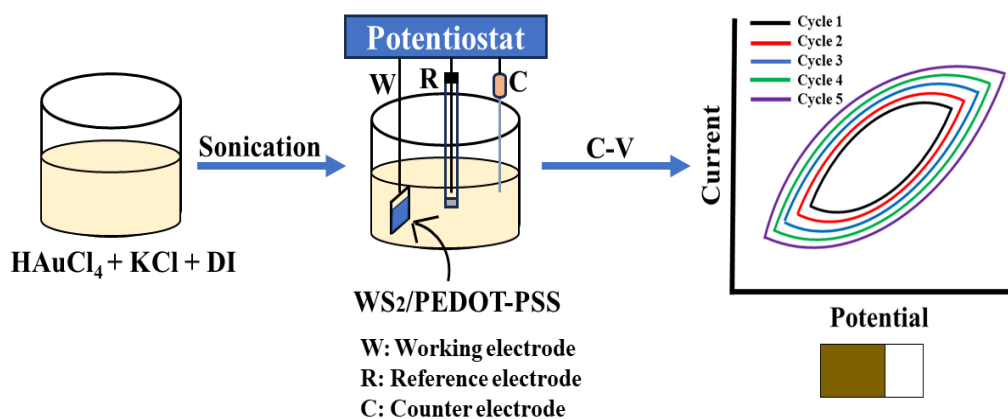


Figure 2.11: Schematic illustration of preparation of $\text{Au}/\text{WS}_2/\text{PEDOT-PSS}/\text{ITO}$ electrode.

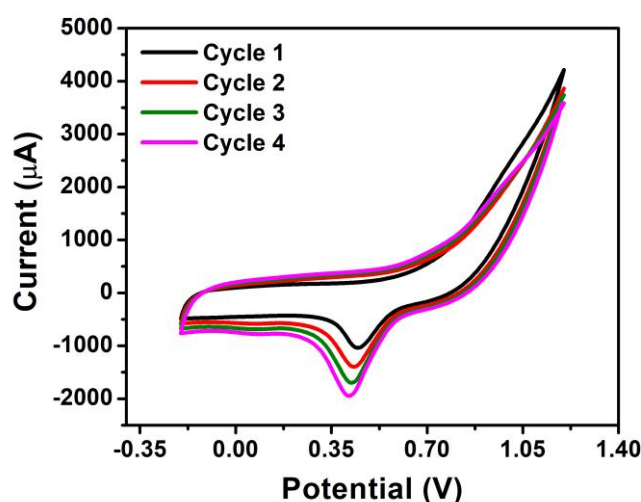


Figure 2.12: Deposition curves of Au/WS₂/PEDOT-PSS/ITO electrode within the potential window from – 0.2 V to 1.2 V.

By executing CV up to 4 cycles with a potential window of -0.2 V – 1.2 V and scan rate of 20 mV/s, AuNPs were electrochemically deposited over the surface of the fabricated WS₂/PEDOT-PSS/ITO electrode. The deposition CV curves of AuNP/WS₂/PEDOT-PSS over the ITO electrode can be found in Figure 2.12.

2.4. Mechanism behind electrochemical polymerization and electrode fabrication

Electro- polymerization of EDOT monomer in presence of PSS and 2D material (GO, WS₂) was carried out through cyclic voltammetry. CV was recorded by taking a potential window from - 0.2 V to 1.2 V and 20 mV/s of scan rate in a three- electrode setup comprising of a reference electrode (Ag/AgCl), platinum (Pt) as a counter electrode and bare ITO as a working electrode. During the electrochemical polymerization process in presence of 2D material, first the monomer EDOT is oxidized to a cationic radical by stripping of one electron from EDOT which is represented in equation 2.1,



EDOT in its oxidized form (EDOT⁰⁺) has a strong affinity for the negative charges present in the solution. Being a negative dopant, the PSS chain interacts with the thiophene ring present in EDOT. GO consists lots of negatively charged functional groups over its edges and basal plane. So, these cationic EDOT⁰⁺ radicals can easily get attached over the GO sheets in the solution. Again, there are a number of negative charges present in the edges and the basal planes of WS₂ as well. It should be noted that EDOT⁰⁺ radicals that interact

with 2D sheets and PSS side chains get transformed into PEDOT-PSS together with stacked 2D layers (GO, WS₂) in between the polymer chains having Van der Waals interaction between 2D layers and thiophene ring. The deposition curves of GO/PEDOT-PSS/ITO and WS₂/PEDOT-PSS/ITO electrode is shown in Figure 2.5 and Figure 2.10 respectively. With each cycle the area under the CV curve is found to be increased due to increased conductivity and capacitance. The area under the CV curve is related to the quantity of charge exchanged during the redox reaction. If the conductivity and capacitance increase with each cycle, it can affect the shape and size of the CV curve. Specifically, an increase in conductivity facilitates faster electron transfer between the electrode and the electrolyte species and leads to higher current response. While an increasing capacitance suggests more charge can be stored at the electrode-electrolyte interface. This allows for greater charge accumulation and redistribution during the CV scan, leading to a larger area under the curve. As the area under the CV curve is increasing with each cycle, it suggests that more charge is being exchanged during the redox reaction. This could be due to several factors, such as improved electrode kinetics, increased surface area of the electrode, or changes in the properties of the electrolyte. Electro - deposition curves of AuNPs anchored GO/PEDOT-PSS and WS₂/PEDOT-PSS over ITO electrode can be found in Figure 2.7 and Figure 2.12 respectively. Interestingly, when stable, chemically inert AuNPs are introduced into the system, a passive layer could form, which would eventually increase the current even more. One reduction peak is clearly observed at around 0.4 V for both the electrodes AuNP/GO/PEDOT-PSS and AuNP/WS₂/PEDOT-PSS (Figure 2.7 and Figure 2.12) respectively due to the reduction of Au from Au (3+) to Au (0) [11-13], which gives evidence of the presence of AuNPs layers over the polymer-2D material composite surface.

2.5. Synthesis steps and optimization-system III (PANI-PVA)

2.5.1. Polyaniline powder

Polyaniline (PANI) can be synthesized by utilizing several techniques both chemically and electrochemically. Here, PANI has been prepared by chemical oxidative polymerization of aniline monomer [14, 15]. In a typical polymerization reaction, 2 g aniline was dissolved in an acidic medium, 50 mL of HCl (1 M) with constant stirring at room temperature to form aniline hydrochloride solution.

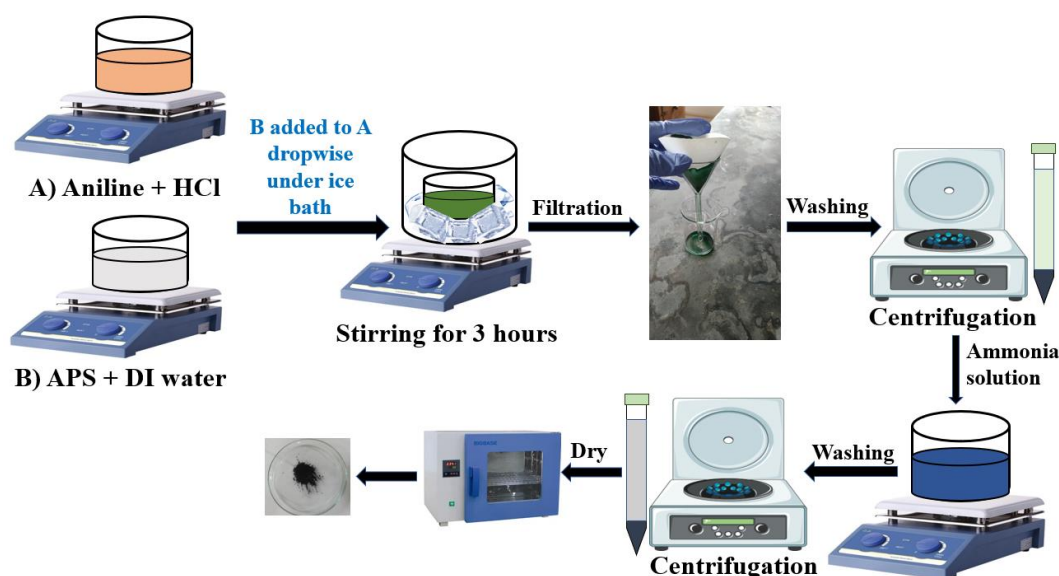


Figure 2.13: Schematic illustration of chemical synthesis of polyaniline (PANI).

The mixture was then cooled down to 0 °C in an ice bath. Another solution of 4 g ammonium peroxydisulfate (APS) in 20 ml of DI water was prepared and added dropwise to the aniline solution maintaining 0 °C temperature under constant stirring. After the completion of APS solution addition, the mixture was incubated under stirring for 3 h at –5 to 0 °C. During the polymerization process, the colour changed to dark green. The resulting doped PANI precipitate (emeraldine salt) was washed with deionized water and absolute ethanol several times. To prepare dedoped PANI (emeraldine base), doped PANI precipitate was dissolved in 50 ml of 1 M aq. ammonia solution, with stirring for 24 h at room temperature, and filtered. The wet powder was washed thoroughly with deionized water and dried at 50 °C to obtain emeraldine base, denoted as dedoped PANI hereafter. Emeraldine (EM) base is regarded as the most useful form of polyaniline due to its high stability at room temperature and from literature it is found that the baseline of the dedoped PANI nanofiber sensor is more stable than the doped sensor. Additionally, the dedoped nanofiber sensor has better repeatability and stability than the doped sensor.

2.5.2. PANI nanofibers

PANI nanofibers can be synthesized by using various methods like soft template method, hard template method [16], dilute polymerization [17], seeding polymerization [18], interfacial polymerization [19], electrospinning [20] and ultrasonic irradiation [21].

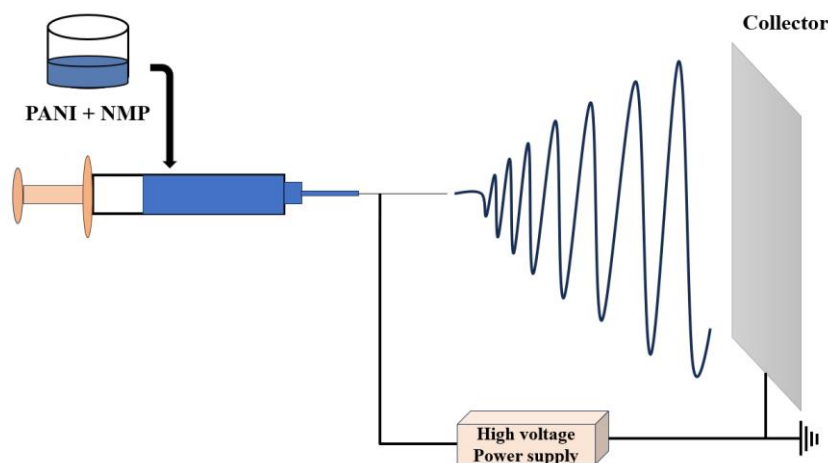


Figure 2.14: Schematic illustration of preparation of PANI nanofibers.

Among all, electrospinning is the most favourable and versatile method to get an abundance of ultrathin uniform fibers [22]. To prepare PANI nanofibers through electrospinning, initially 0.04 g dedoped PANI was dissolved in 4 ml N-Methyl-2-pyrrolidone (NMP) with constant stirring for 3 h until a clear viscous solution was observed. NMP was used to dissolve polyaniline due to its good solvency properties for making the solution for electrospinning [23]. The homogeneous solution was then transferred to a syringe, and the electrospinning was performed at 19.2 kV with a 12 cm distance between two electrodes with RPM 960 [24]. The collected sample was dried in an oven at 50 °C for 3 h.

2.5.3. PANI-PVA solution

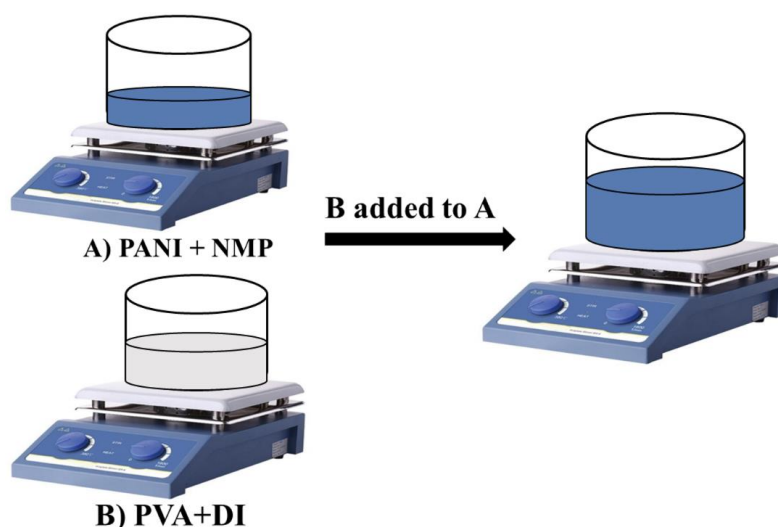


Figure 2.15: Schematic illustration of preparation of PANI-PVA composite solution.

The primary step involved preparing a 10wt% PVA aqueous solution [25]. In another container, 0.01 g dedoped PANI was dissolved in 1 ml NMP with constant stirring for 3 h until thoroughly dissolved and then filtered. Afterwards, the PVA solution was added to the PANI solution in different ratio for optimization. The obtained mixture was then left overnight for stirring to yield a homogenous solution.

2.5.4. PANI-PVA nanofibers

The resulting viscous solution of PANI-PVA was then transferred to a syringe and the electrospinning was performed at 16 kV with a 10 cm distance between two electrodes with RPM 980 [26]. Schematic illustration for preparation of PANI-PVA nanofibers is shown in Figure 2.16. Fine electrospun fibers were successfully collected on the Al foil (thickness: 15 micron). The collected sample was dried in an oven at 50 °C for 3 h. Two snapshots are shown below in Figure 2.17 which was captured during the experiment.

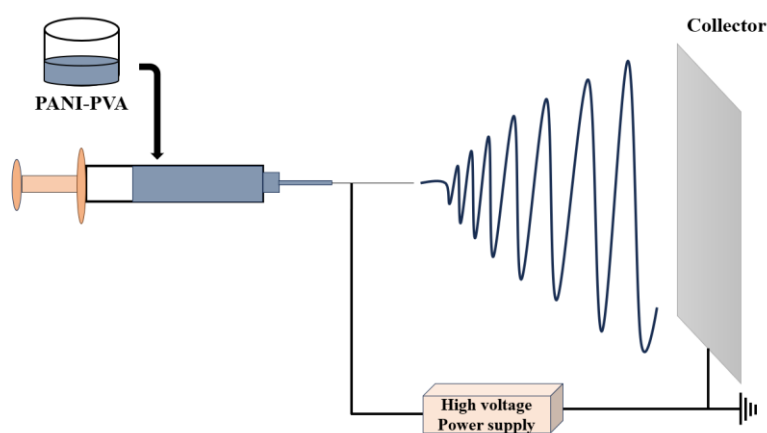


Figure 2.16: Schematic illustration of preparation of PANI-PVA nanofibers.

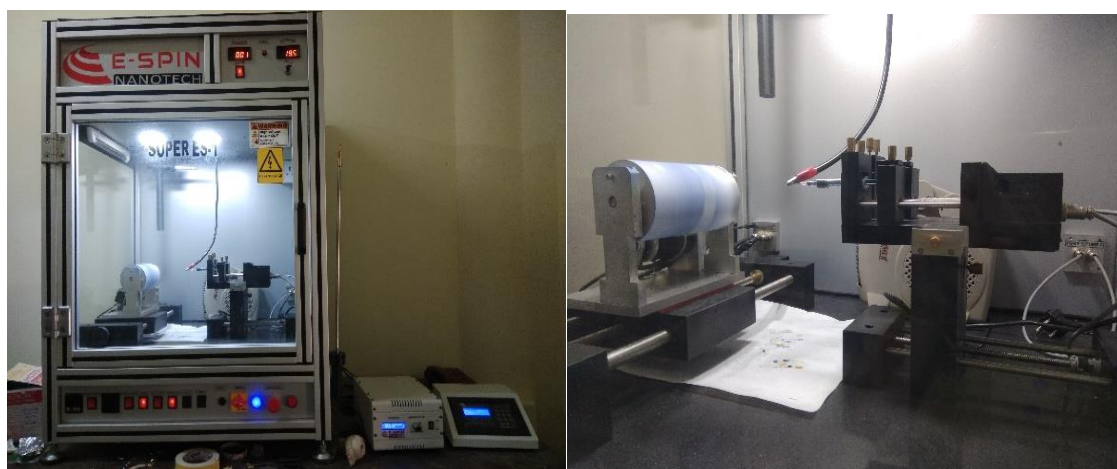


Figure 2.17: Electrospinning unit during experiment.

2.6. Nano-bio interface and biofunctionalization

2.6.1. Preparation steps of enzymatic Glucose sensors

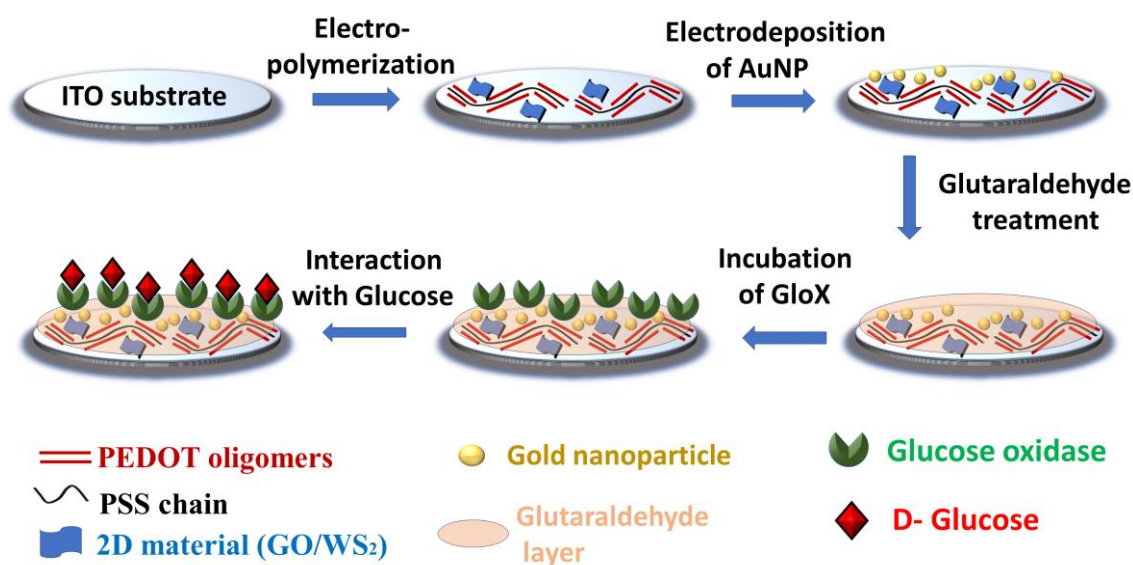


Figure 2.18: Schematic illustration of the AuNP anchored 2D (GO or WS₂) modified PEDOT-PSS/ITO based glucose sensor.

Prior to all, the synthesized AuNPs anchored GO/PEDOT-PSS/ITO, AuNP/WS₂/PEDOT-PSS/ITO, PANI-PVA electrodes were dipped with glutaraldehyde (2% W/V) for a time period of 1 h [27]. Glutaraldehyde is a dialdehyde with two highly reactive aldehydic groups which can bind covalently with different functional groups such as hydroxyl, amine, phenol, thiol etc. [28]. Upon glutaraldehyde treatment, the amine group present in PANI and hydroxyl groups of PSS and graphene oxide react with the aldehydic group to form covalent linkage [29, 30]. After treatment with glutaraldehyde, the modified electrodes were washed twice with PBS to detach the unbounded glutaraldehyde from the surface of the electrodes. Afterwards, the films were incubated in 3 mg mL⁻¹ of glucose oxidase enzyme (*GLOx*) and stored almost for 4 h at a temperature of 4 °C. Then the bioelectrodes were carefully washed with PBS solution to eliminate the weakly bound enzyme. The developed *GLOx*/GLU/AuNP/GO/PEDOT-PSS/ITO, *GLOx*/GLU/AuNP/WS₂/PEDOT-PSS/ITO and *GLOx*/PANI-PVA/ITO electrodes were used for further sensing experiments. Schematic of sensor fabrication of PEDOT-PSS functionalized 2D layered material decorated with gold (Au) nanoparticles towards glucose detection is shown in Figure 2.18, while schematic for PANI-PVA nanofibers based glucose sensor can be found in Figure 2.19.

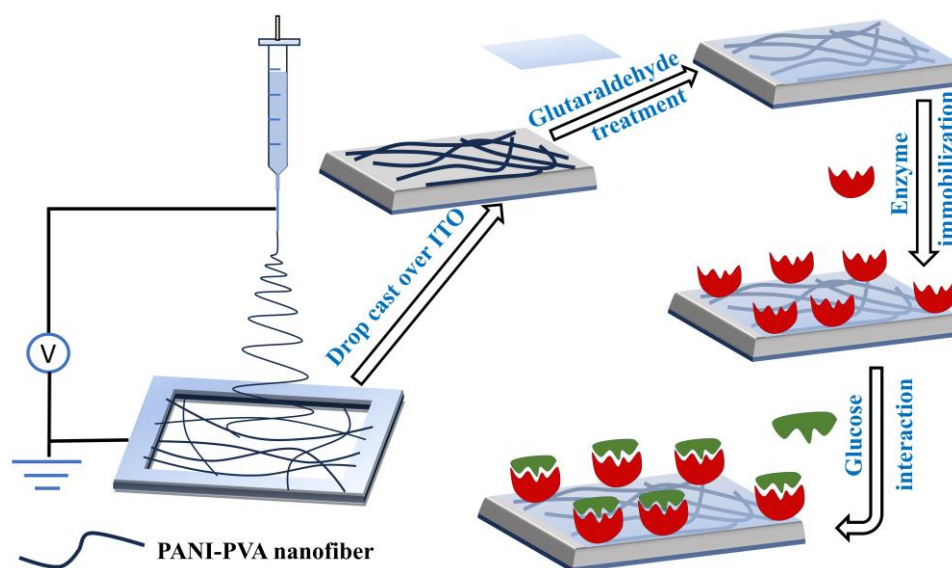


Figure 2.19: Schematic illustration of the PANI-PVA nanofiber based glucose sensor.

2.6.2. Preparation of Aflatoxin B₁ sensors

In the same way, the synthesized AuNP/GO/PEDOT-PSS, AuNP/WS₂/PEDOT-PSS and PANI-PVA nanofibers based electrode were immersed in (2% W/V) glutaraldehyde for 1 h. To detach the unbounded glutaraldehyde, the GLU/AuNP/GO/PEDOT-PSS, GLU/AuNP/WS₂/PEDOT-PSS and GLU/PANI-PVA electrodes were washed with PBS. Subsequently the electrodes were incubated with an antibody (200 $\mu\text{g mL}^{-1}$) anti-AF-B₁ for 1 h at room temperature. To remove the weakly bonded antibody all the bioelectrodes were thoroughly rinsed with PBS. To block the nonspecific sites on the electrode, 1 mg mL⁻¹ solution of BSA was added and kept for 1 h. Later, films were washed with PBS to remove the excess BSA and stored at 4 °C for further experiment. The schematic of the AF-B₁ sensor preparation for AuNP/2D/PEDOT-PSS is displayed in Figure 2.20 and for PANI-PVA based nanofibers the schematic of the sensor fabrication can be found in Figure 2.21.

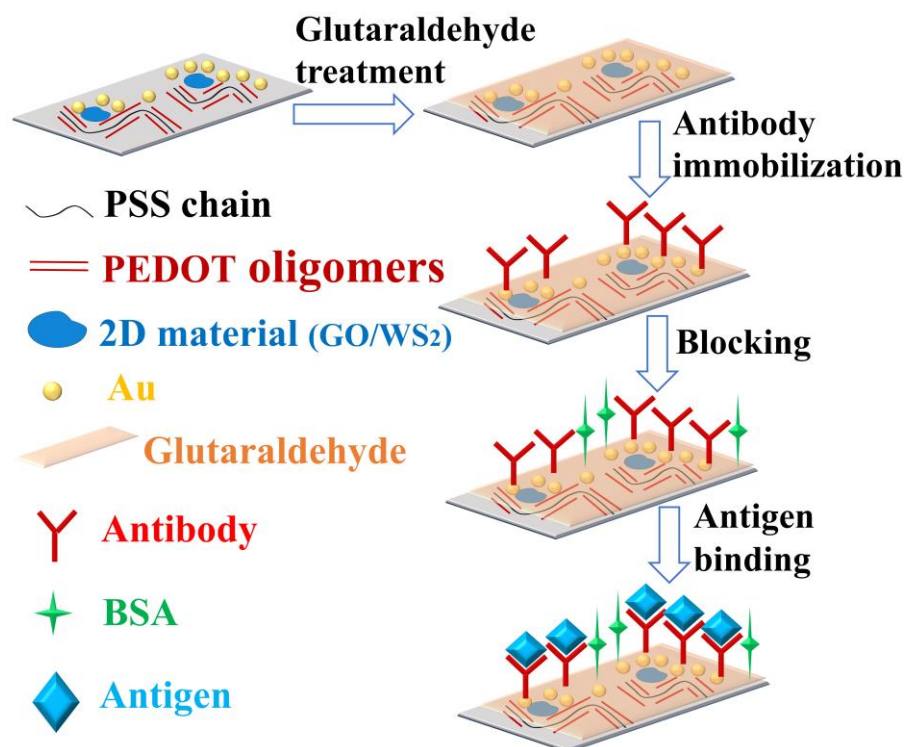


Figure 2.20: Schematic of electrochemical based immunosensor (AuNP/2D/PEDOT-PSS) fabrication and testing.

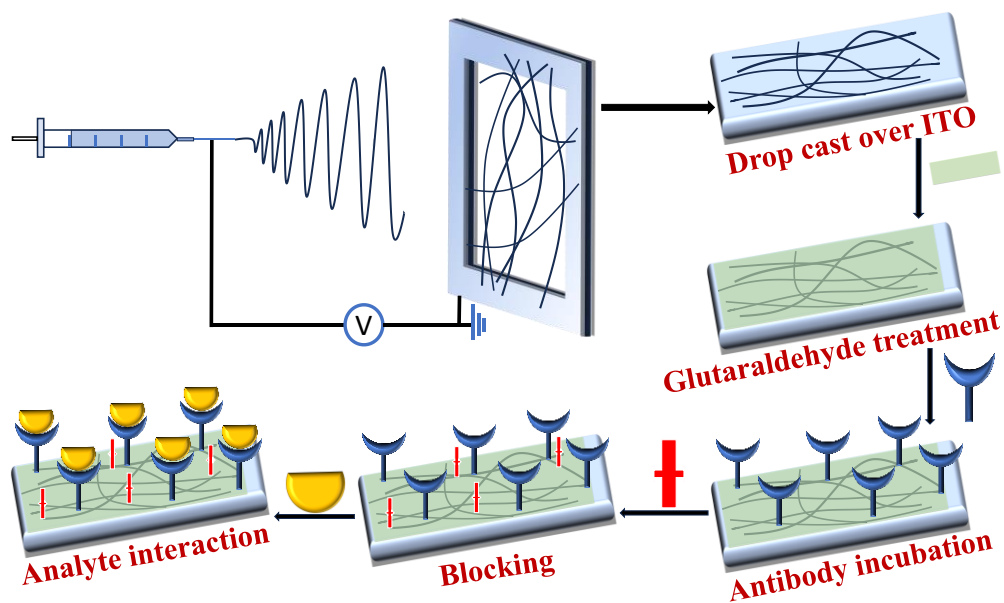


Figure 2.21: Schematic of electrochemical based immunosensor (PANI-PVA) fabrication and testing.

2.7. Analytical tools and techniques

2.7.1. X-ray diffraction (XRD)

X-ray diffraction (XRD) is an analytical technique which is commonly used to study the crystal structure, phase identification and crystallinity of materials. The diffraction pattern produced by X-rays furnishes broad insights into structural characteristics such as lattice constants, d-spacing, average crystallite size, diffraction planes, defects, and the percentage of crystallinity within the material [31]. Within the X-ray tube, electrons are produced through thermionic emission, originating from a tungsten filament upon the application of approximately 40 kV potential. Since a high voltage is maintained across the electrodes, electrons are drawn toward the anode, typically composed of a metal target, such as copper. When electrons collide with the copper target, they cause the ejection of electrons from the 1s orbital of copper. As a result, 2p electrons transition to fill the empty space, leading to the emission of energy in the form of X-rays with a wavelength of 0.154056 nm [32]. The X-rays undergo filtration to achieve monochromatic radiation, are collimated, and then directed towards the sample. In X-ray diffraction, electromagnetic waves interact with the atoms within the crystal lattice [31]. Upon exposure of a crystalline material to a monochromatic X-ray beam, the incoming x-ray photons interact with the surrounded electrons of the atom leads to scattering in all directions. XRD peaks arise from the constructive interference of monochromatic X-rays scattered at particular angles by the lattice planes present in the sample. When incident X-rays obey Bragg's law, they undergo constructive interference, resulting in the observation of a peak in intensity. According to Bragg's law [33,34],

$$n\lambda = 2d \sin \theta \quad (2.2)$$

Here, n is an integer representing the diffraction pattern order, d signifies the interplanar spacing, λ stands for the incident X-ray wavelength, and θ denotes the incident angle. Throughout the experiment, a detector captures the diffracted patterns generated by the interaction of X-rays with the crystal lattice. The detector measures the intensity of diffracted X-rays across different angles, forming a distinct diffraction pattern. The gathered data is subsequently analyzed to transform intensity measurements into a count rate, indicating the quantity of X-rays detected per unit time. All collected processed diffraction data as count rates, is displayed in a monitor. The XRD measurements were carried out using EMPYREAN diffractometer platform with monochromatic Cu K α

radiation having wavelength 1.54056 \AA with an accelerating voltage of 40 mV and current 45 mA and $0.1^\circ \text{ min}^{-1}$ scan rate at Gauhati University and a D8 Bruker AXS X-ray diffractometer at Tezpur University with an operating voltage of 40 mV and current 45 mA and scan rate of 1° min^{-1} .

2.7.2. Fourier Transform Infrared Spectroscopy (FTIR)

Fourier Transform Infrared Spectroscopy (FT-IR) serves as an analytical tool for identification of various functional groups, chemical bonds, and molecular structures within a material. Infrared spectroscopy deals with the interactions between molecular vibrations and electromagnetic radiation within the infrared spectrum. Infrared (IR) spectroscopy operates on the principle that the functional groups within a molecule absorb distinct frequencies of vibration. Typically, the infrared (IR) spectrum is categorized into the near-infrared ($13000\text{--}4000 \text{ cm}^{-1}$) regions, mid-infrared ($4000\text{--}400 \text{ cm}^{-1}$) and far infrared ($<400 \text{ cm}^{-1}$) [35]. To qualitatively analyze molecules, the medium infrared region (MIR) is preferred, as it enables the detection of signals corresponding to the vibrational frequencies aligned with mid-infrared radiation frequencies, facilitating molecule identification. Within the mid-infrared spectrum, there exists a division into the functional group region ($4000\text{--}1800 \text{ cm}^{-1}$) and the fingerprint region ($1800 \text{ to } 400 \text{ cm}^{-1}$). The initial region pertains to the IR active stretching frequencies of molecular compounds, while the second region corresponds to vibrational frequencies associated with specific combinations of molecular moieties' vibrational modes. When exposed to infrared radiation, a material selectively absorbs distinct frequencies of vibration depending on the type/nature of molecular bonds present in the material. When subjected to infrared radiation, a molecule experiences changes in its dipole moment, leading to the potential for excitation to higher vibrational or rotational state within the same electronic band. The frequency of absorption correlates with the vibrational frequency of the molecules, whereas the intensity of absorption is determined by the degree of change in their dipole moment. The distinct energy associated with bending or stretching modes is expressed in units of wavenumber. Hence, an infrared spectrum serves as a unique feature of the chemical composition of a sample with absorption peaks that align with the vibrational frequencies of the molecular bonds within the material. Because the atomic configuration varies between materials, each compound possesses a distinct IR spectrum, enabling IR spectroscopy to differentiate between various chemical species.

FTIR spectroscopy of the samples was conducted using a Perkin Elmer Spectrum 100 spectrophotometer, installed at Tezpur University in Assam, India. The samples were prepared by pressing them with standard potassium bromide (KBr) into pellet form. The spectra were recorded over a range of 400-4000 cm^{-1} with a resolution of 1 cm^{-1} .

2.7.3. Field emission scanning electron microscope (FE-SEM)

A field emission scanning microscope employs a high energy electron beam to scan the sample surface. In FESEM, the interaction of the liberated electrons with the atoms within the sample gives the compositional and morphological information in as small as nanometer range. The field emission gun generates highly accelerated primary electrons characterized by a high current density within the vacuum column. In conventional electron microscopes, electrons are predominantly emitted from a tungsten single crystal featuring a needle-shaped tip, achieved through the application of current, raising its temperature to approximately 2800°C. A tungsten filament holder incorporating a crystal of lanthanum hexaboride (LaB6) serves as an electron source to enhance resolution. In a field emission (FE) scanning electron microscope, a "cold" source is utilized instead of heating, eliminating the need for heating elements [36,37].

The electrons cloud free from their source undergo acceleration within a strong electrical field gradient of a high vacuum environment ranging from 10^{-4} to 10^{-10} Torr. Electronic lenses deflect the concentrated electrons to generate a highly intense beam, which interacts with the sample. The interaction between the electron beams and the sample occurs in both elastic and inelastic manners, resulting in different signals. These signals include secondary electrons (SEs), back-scattered electrons (BSEs), transmitted electrons (TEs), and characteristic X-rays, all of which are detected by a scintillation photomultiplier detector. To visualize surface morphology and roughness, primary secondary electrons (SE) are considered due to their ability to precisely pinpoint the exact location of the beam on the sample surface providing detailed morphological information with a very high resolution [38]. Secondary electrons are emitted from the k-shell of atoms through inelastic scattering interactions with the incident electron beam. When the electron beam undergoes elastic scattering upon interacting with the specimen surface, it produces backscattered electrons. These electrons are used for the purpose of elemental analysis. Backscattered electrons originate from deeper regions within the specimen which gives

valuable details about its elemental compositions [39,40].

FESEM imaging was carried out using a FESEM Zeiss sigma 300, installed at Tezpur University, Assam, India and Carl ZEISS Sigma 300 VP, procured from Germany, Installed at Gauhati University. The micrographs were captured using an accelerating voltage ranging from 5 to 15 kV, with the magnification set as required, spanning from 5,000X to 50,000X. To investigate the surface morphology of fresh and stored real biological samples, a JEOL JSM 6390 LV model scanning electron microscope has been used.

2.7.4. Evaluation of electrochemical properties using Potentiostat

The basic elements of an electroanalytical system for voltammetry include a potentiostat, the electrochemical cell and a computer. It is the potentiostat's role to apply a known potential and observe the corresponding current. The fundamental components of a potentiostat comprise a cell and electrodes. A standard electrochemical cell typically comprises three electrodes, along with the sample dissolved in a solvent containing an ionic electrolyte. Depending on the particular application, the nature of samples, and the required analytical information, different cells (or sample containers) have different configurations, sizes, and materials. Materials like glass, teflon, and polyethylene, for instance, are used to minimise possible cross reactions between the sample and the cell. The details about all the three electrodes are given below,

- a) Working electrodes: The working electrode controls the potential and measures the current. Depending on the application, the working electrodes can be made of various materials, ranging from flat Pt discs to tiny Hg drops. ITO electrode is one of the widely used working electrodes in electrochemistry due to its various properties like excellent substrate adhesion, wide working window, good optic transparency, high electrical conductivity and stable physical and electrochemical features [41]. ITO sheet is typically used because it is comparatively less expensive than other traditional electrodes like gold, nickel, mercury, and platinum [10, 42].
- b) Counter electrodes: In a two electrode setup, the counter electrode has two purposes. Firstly, it completes the circuit facilitating charge transfer through the cell. Additionally, it ensures a consistent interfacial potential, independent of the current flow. Meeting both of these requirements simultaneously is typically not

possible under most cases. It is difficult to keep a steady counter electrode potential in a two electrode system while current is flowing. Due to this fact, along with the absence of voltage drop compensation across the solution, controlling the working electrode potential becomes challenging in a two-electrode system, resulting in poor performance. Two distinct electrodes are better suited for the roles of conducting current and maintaining a standard reference voltage separately. So, in the case of three electrode systems, the counter electrode is used to carry current and to complete the circuit. In many cases of voltammetric procedures, isolating the counter electrode from the sample species is typically not required since the analytical processes at the electrode surfaces take place over an extremely short period of time. Mostly, the counter electrodes are made up of thin platinum wire, although sometimes graphite and gold can also be used.

- c) Reference electrodes: In case of two-electrode systems, there is a current flow between the working electrode and counter electrodes, but to determine the potential at which the reaction occurs can be challenging, hence there is a necessity of another standard electrode. The reference electrode should be simple to manufacture and maintain, have a steady half-reaction (reversible) with Nernstian behaviour. Most commonly employed reference electrodes for aqueous solutions include the silver/silver chloride electrode (Ag/AgCl) and the calomel electrode. Their potentials are determined by the given reactions, $\text{Hg}_2\text{Cl}_2 (\text{s}) + 2\text{e}^- = 2\text{Hg} (\text{l}) + 2\text{Cl}^-$ and $\text{AgCl}(\text{s}) + \text{e}^- = \text{Ag}(\text{s}) + \text{Cl}^-$. The reference electrode should ideally be positioned as close to the working electrode as feasible; nevertheless, in certain situations, it could be required to keep the reference electrode away from the working electrode in order to prevent contamination [43]. Electrochemical analyses were conducted using a potentiostat/galvanostat (Gamry, model: 992-00129, Mumbai, India) in a three-electrode system comprising of reference electrode (Ag/AgCl), counter electrode (platinum), and polymer composite electrode as working electrode. Indium tin oxide (ITO) modified electrocatalyst served as a working electrode.

2.7.4.1. Cyclic Voltammetry (CV)

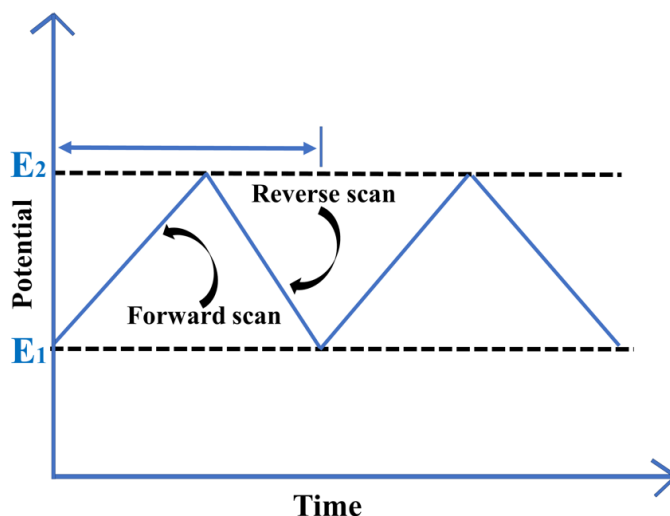


Figure 2.22: Triangular potential waveform used in cyclic voltammetry showing the variation of potential from an initial value (E_1) to a final value (E_2).

Cyclic voltammetry is an electroanalytical method used to study the electrochemical performance of a system revealing both the application oriented or fundamental information [44]. In 1938, CV was first reported and Randles and Sevcik introduced the theory of cyclic voltammetry for the first time in 1948 [45-48]. This approach is often used to get qualitative information on electrochemical cell reactions and their corresponding potential at which they occur. Cyclic voltammetry serves as the primary method to obtain qualitative insights into electrochemical redox reactions, including mass transport activity, heterogeneous electron transfer kinetics, thermodynamics of redox reactions, and adsorption processes. A cyclic voltammogram is obtained by applying a predefined fixed linear potential to an electrode immersed in a solution, gradually scanning from an initial potential to a final potential value, either increasing or decreasing over time which leads to a current voltage plot. In CV measurements, a triangular waveform potential is typically applied to the working electrode, while recording the resulting current response. At the working electrode, the potential initiates at a specific value, such as E_1 , and it scans over a specified duration to reach the final potential, E_2 . The cyclic voltammogram is then completed by reversing the scan to the beginning potential, E_1 , can be found in Figure 2.22. The appearance of oxidation and reduction peak during a CV cycle is shown in Figure 2.33.

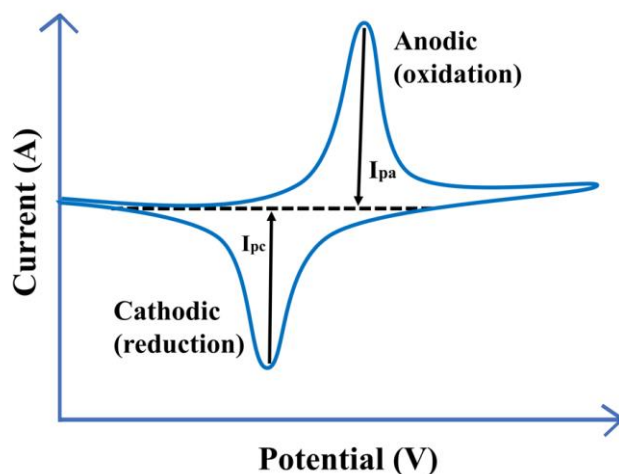


Figure 2.23: The cyclic voltammogram of a Nernstian electrochemical reaction.

In the cyclic voltammogram, the upper section indicates oxidation with a maximum current referred to as the anodic peak current (i_{pa}) while the bottom half signifies reduction, where the maxima current is known as cathodic peak current (i_{pc}) respectively. The number of cycles and scan rate can be varied during CV. At slower scan rates, electrolyte ions can have sufficient time to penetrate the electrode pores, while at higher rates, ions tend to accumulate only at the surface of the electrode. Additionally, the faradaic reactions occurring on the surface of the electrode are unable to keep up with rapid fluctuations in electrode potential, leading to incomplete reactions and poor output current. This phenomenon results in a decrease in capacitance at higher scan rates. In our experiment, a scan-rate of 20 mV/s is kept constant during the cycle. The cyclic voltammetry measurements were conducted using a Gamry Interface potentiostat in presence of a three-electrode setup, employing Ag/AgCl as the reference electrode and platinum as the counter electrode and synthesized conducting polymer nanocomposite deposited electrode as a working electrode. Various electrolytes, including phosphate-buffered saline (PBS) and mixture of ferri/ferrocyanide $[\text{Fe}(\text{CN})_6]^{3-/4-}$ and PBS, were utilized at different stages of the experiments.

2.7.4.2. Electrochemical Impedance Spectroscopy (EIS)

Electrochemical Impedance spectroscopy (EIS) is one of the powerful tools to study the different kinds of electrochemical, chemical and surface processes at the electrodes and electrolyte and interfaces [49]. Additionally, it is utilised to investigate the formation of electric double layers, charge transfer at the electrode-electrolyte interface, kinetics of

charge transport in electrode materials, and electrode and electrolyte dielectric behaviour. In EIS, the potential of the electrode is perturbed from its equilibrium state by employing a small sinusoidal potential (typically within the amplitude range of 2-10 mV) in an electrochemical cell across a wide frequency range from 10^{-4} Hz to 10^8 Hz [50]. This perturbation results in a sinusoidal current signal with the same frequency but exhibits a different phase angle from the applied potential. The input sinusoidal potential and the corresponding response current signal of the electrochemical cell is illustrated in Figure 2.24. The phase difference between the response signal and the input signal across a wide range of frequencies is highly useful for investigating various electrode processes, such as the formation of the electric double layer (EDL), charge transfer kinetics in electronic, or ionic, or mixed conductors, diffusion of the redox species, and both homogeneous and heterogeneous charge transfer kinetics [51]. Impedance, which is measured in Ohms (Ω), is the obstacle that an electrical system provides towards the flow of charge carriers. When there is no phase difference between the input potential and the resulting electric current, it is called resistance, which does not vary with frequency means it is independent of frequency. Therefore, Ohm's law is applicable under these conditions:

$$E = IR, \quad (2.3)$$

Where, E represents the input potential in Volt (V), R is the resistance and I represent the current which is in ampere (A). When a sinusoidal potential is subjected to an electrochemical cell composed of resistors, capacitors, or inductors, a phase difference occurs between the resulting current flowing through the circuit and the applied potential. Therefore, the alternating potential $E(t)$ and current $I(t)$ can be represented as [52]:

$$E(t) = E_0 \sin(\omega t) \quad (2.4)$$

$$I(t) = I_0 \sin(\omega t + \phi) \quad (2.5)$$

where, E_0 represent amplitudes of potential, I_0 is the amplitude of current and ω represent the angular frequency which can be expressed as $\omega = 2\pi f$, where f represents the frequency, ϕ denotes the phase shift of the measured current signal with respect to applied potential, and t indicates time.

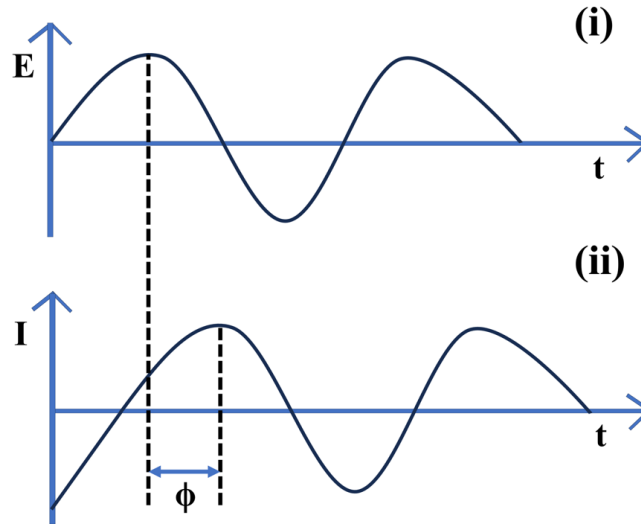


Figure 2.24: (i) The input sinusoidal potential and (ii) corresponding current signal in output of the electrochemical cell.

The relationship between input potential and output current is known as the electrochemical impedance (Z), and it may be described in terms of phase difference (φ) and magnitude (Z_0):

$$Z(\omega) = \frac{E(t)}{I(t)}$$

$$Z(\omega) = \frac{E_0 \sin(\omega t)}{I_0 \sin(\omega t + \varphi)}$$

$$Z(\omega) = Z_0 \frac{\sin(\omega t)}{\sin(\omega t + \varphi)} \quad (2.6)$$

By considering both $E(t)$ and $I(t)$ in the complex plane, they can be represented as:

$$E(t) = E_0 \exp(j\omega t) \quad (2.7)$$

$$I(t) = I_0 \exp[j(\omega t + \varphi)] \quad (2.8)$$

Where j represents an imaginary number and can be defined as $j = \sqrt{-1}$.

The impedance (Z) may be expressed in complex form using the Euler's relation which is,

$$\exp(j\theta) = \cos \theta + j \sin \theta$$

Now,

$$Z(\omega) = \frac{E_0 \sin(j\omega t)}{I_0 \sin [j(\omega t + \varphi)]}$$

$$Z(\omega) = Z_0 \frac{\sin(j\omega t)}{\sin [j(\omega t + \varphi)]}$$

$$Z(\omega) = Z_0 \exp(-j\varphi)$$

$$Z(\omega) = Z_0 \exp (\cos \varphi - j \sin \varphi)$$

$$Z(\omega) = Z' + j (-Z'') \quad (2.9)$$

Therefore, the total impedance can be expressed as sum of the real component (Z') and imaginary component (Z''). A vector of length $|Z|$ may be used to represent the magnitude of the impedance, while the phase angle, φ , indicates the anticlockwise angle between this vector and the X-axis.

The magnitude of Z can be expressed as:

$$|Z(\omega)| = \sqrt{(Z')^2 + (-Z'')^2} \quad (2.10)$$

and the phase angle is given by:

$$\varphi = \tan^{-1} \frac{Z''}{Z'} \quad (2.11)$$

In impedance analysis, the real component represents resistance, while the imaginary component, known as reactance, arises from the 90-degree phase shift between voltage and current [53]. Depending on the phase difference between voltage and current, reactance divides into two categories: one is inductive reactance (X_L) and other is capacitive reactance (X_C). For inductors, $X_L = \omega L$, where L represents the inductance, however for capacitive elements, X_C is negative and may be expressed as $X_C = -1/\omega C$, where C represents the capacitance. Plotting Z' on the X-axis and Z'' on the Y-axis yields the corresponding impedance spectra, which is referred to as a Nyquist plot and can be found in Figure 2.25(a).

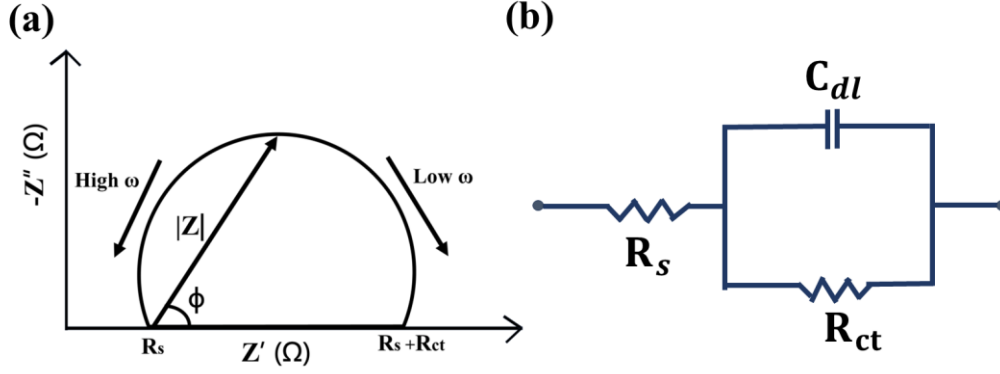


Figure 2.25: (a) Nyquist plot and (b) corresponding simplified Randles equivalent circuit.

On the Nyquist plot, the Y-axis is oriented negatively, with each point representing the impedance at a particular frequency [54]. The Nyquist plot which is utilized for analyzing electrochemical processes and may be thought of as an equivalent electrical circuit model, which includes components such as resistors, capacitors and inductors. By fitting the experimental data to the electrical circuit model, one can obtain the exact value of a few commonly used parameters like solution resistance (R_s), double layer capacitance (C_{dl}), charge transfer resistance (R_{ct}) and many more [55]. The most often used circuit model to fit the Nyquist plot is the simplified Randles equivalent circuit shown in Figure 2.25 (b).

The total impedance in Randles equivalent circuit can be represent as [56,57]:

$$Z(\omega) = R_s + \frac{R_{ct}}{1 + \omega^2 R_{ct}^2 C_{dl}^2} - j \frac{\omega R_{ct} C_{dl}}{1 + \omega^2 R_{ct}^2 C_{dl}^2}, \quad (2.12)$$

where the real component of impedance is

$$Z'(\omega) = R_s + \frac{R_{ct}}{1 + \omega^2 R_{ct}^2 C_{dl}^2} \quad (2.13)$$

and the imaginary component is given as

$$Z''(\omega) = - \frac{\omega R_{ct} C_{dl}}{1 + \omega^2 R_{ct}^2 C_{dl}^2} \quad (2.14)$$

At higher frequency ($\omega \rightarrow \infty$), the frequency-dependent terms in equation (2.12) diminish, leading to $Z(\omega) = R_s$. Therefore, at high frequencies, the phase angle is zero and the impedance becomes purely resistive, indicated by the intercept on the real axis. On the other hand, at low frequencies ($\omega \rightarrow 0$), $Z(\omega) = R_s + R_{ct}$ and it is determined by the real axis intercept at lower frequency side of Nyquist plot.

Considering ω_{max} as the frequency at which the imaginary component of impedance, $-Z''(\omega)$, reaches its maximum value.

Hence, for the maximum value of $-Z''(\omega)$, [58]

$$\omega_{max} R_{ct} C_{dl} = 1 \quad (2.15)$$

Hence, C_{dl} can be expressed as [58]:

$$C_{dl} = \frac{1}{\omega_{max} R_{ct}} \quad (2.16)$$

The non-ideal performance of C_{dl} primarily arises from an inhomogeneous electrode surface caused by surface roughness, the presence of impurities, and the existence of grain boundaries [59]. Therefore, a constant phase element (CPE) can be used in place of a pure capacitor. Furthermore, in cases where the charge transfer kinetics are affected by diffusion processes in an electrochemical system, an additional circuit element called the Warburg impedance is introduced. This element is placed in series combination with R_{ct} [60]. As seen in Figure 2.26 (a), the Warburg element results in a straight line with a 45° slope at the lower frequency region of the Nyquist plot. The complete Randles equivalent circuit in presence of CPE and Warburg impedance element is illustrated in Figure 2.26 (b).

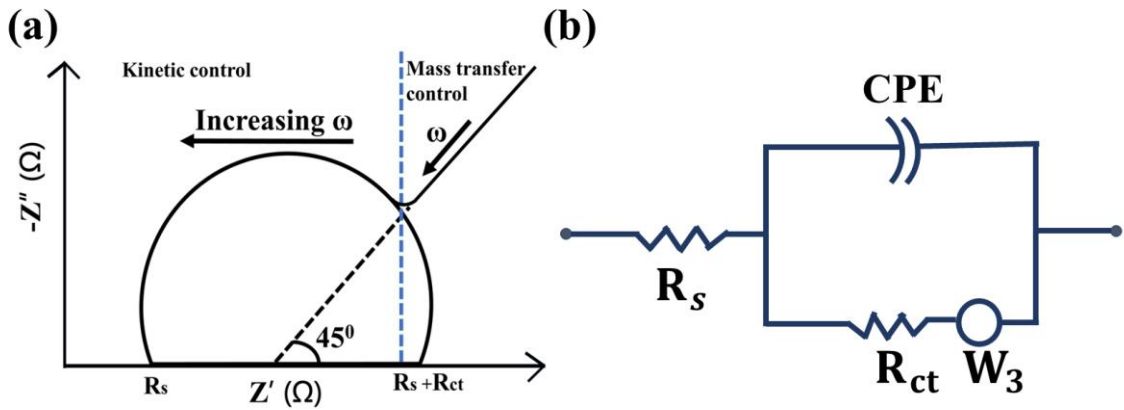


Figure 2.26: (a) Nyquist plot for a mixed circuit and (b) corresponding Randles equivalent circuit.

Various impedance components in an electrochemical cell system:

(a) Solution, or electrolyte resistance (R_s)

The impedance of an electrochemical cell is influenced by the solution resistance between the working electrode and the counter electrode, which arises due to the presence of various species in the solution. Increased ion concentration in the solution reduces resistance. Furthermore, ionic resistance depends not only on the solution concentration but also on the type of ions, temperature, and the geometry of the area containing the electrolyte solution [61]. The solution resistance can be defined as:

$$R = \rho \frac{l}{A} \quad (2.17)$$

In this equation, ρ represents the solution resistivity, l denotes the length, and A indicates area of the solution-containing cell.

(b) Double layer capacitance (C_{dl})

The electrode-electrolyte interface forms an electrical double layer through ion adsorption from the electrolyte solution, accumulation, and rearrangement on the electrode surface. The EDL behaves as a capacitor as it hinders the flow of current. Numerous parameters, including ion concentration, electrode potential, temperature, type of ions, high porosity and roughness of the electrode surface influence the C_{dl} value [62]. Consequently, constant phase elements (CPE) can be used in place of traditional capacitors since electrode-electrolyte interfaces cannot be regarded as perfect capacitors.

The impedance for CPE is provided by [42]:

$$Z_{CPE} = \frac{1}{C_0(j\omega)^n} \quad (2.18)$$

The capacitance is denoted by C_0 , and the exponent is n , with a range of -1 to 1 ($-1 \leq n \leq 1$). Depending on the value of n , the impedance of the constant phase element (CPE) varies, each value carrying distinct physical implications. The CPE is equivalent to a pure resistor when $n = 0$, approaches to a capacitor when n gets closer to 1, and it denotes a perfect capacitor when $n = 1$ [62].

(c) Charge transfer resistance (R_{ct})

The charge transfer resistance (R_{ct}) represents the hindrance to the transfer of charges at the electrode-electrolyte interface and it is related to the kinetics of the reaction. As a result, the R_{ct} value affects the current flow in the electrode. The speed of charge transfer reactions is influenced by a few factors such as the nature of the reaction, the concentration of resultant products, the applied potential, and the temperature.

(d) Warburg Impedance (ω)

The diffusion of charged species through the electrolyte from the bulk solution to the surface of the electrode can also generate an impedance known as Warburg impedance. Warburg impedance is dependent on frequency. ω is high at low frequencies because it takes a long time for the reactants to reach the electrode surface. At high frequencies of potential perturbation, the value of Warburg impedance becomes negligible because the diffusing reactants do not need to travel far [63].

2.7.5. Chronoamperometry (CA)

Chronoamperometry is a key electrochemical technique that involves measuring the response of a working electrode over a wide range of time. This technique provides information about the electrochemical reactions occurring at the electrode surface and the kinetics of these reactions. As the name suggest, this method measures the current response of catalyst by maintaining a steady voltage between the working electrode and the reference electrode as a function of time [64]. The current-time plot generated from chronoamperometry experiments offers valuable information on various electrochemical processes, such as electron transfer kinetics, charge transfer resistance, diffusion coefficients, and reaction mechanisms and adsorption processes. By analyzing the magnitude and shape of the current-time curve one can gain insights about the rate of electrochemical reactions, adsorption and desorption processes, and other electrode activities.

2.7.6. Differential pulse voltammetry

Differential pulse voltammetry (DPV) is a voltametric technique used for electrochemical measurements, particularly in quantitative analysis. Voltammetry refers to current voltage

technique where a varying potential is applied to the working electrode in a three electrode setup with respect to a reference electrode and gives a output current.

In DPV, short pulses (17 ms) with small amplitude (10-100 mV) are superimposed on a linear potential ramp [65] where a base potential value is selected where no faradaic reaction occurs and is then applied to the electrode. The base potential is increased in between pulses with equal increments. The current is measured just before (I_1) and after (I_2) each pulse, and the difference between these currents ($I_2 - I_1$) is recorded. This method effectively reduces the background current caused by the DC ramp, resulting in a Faradaic current that is largely free from capacitive current. The primary advantage of DPV is its low capacitive current, which enhances sensitivity. In electrochemistry, Differential Pulse Voltammetry (DPV) is ideal for detecting and studying chemicals at extremely low concentrations. Consequently, it is widely employed in sensing applications across various industries, including healthcare, food safety, and environmental analysis.

2.7.7. Transient capacitance technique

The transient capacitance technique in electrochemistry is a method which is utilized to examine the electrical properties and interfacial processes occurring at electrode-electrolyte interfaces. It describes the capacitance changes that occur at the interface in response to an applied potential or a perturbation in the system. In transient capacitance technique, a small perturbation voltage is applied to the electrode-electrolyte interface, and the resulting transient current is measured as a function of time. The perturbation voltage usually consists of a small sinusoidal signal or a step voltage applied as a DC bias.

The transient capacitance technique is often used to investigate the kinetics and dynamics of charge transfer reactions at semiconductor-electrolyte interfaces. This method can provide valuable insights into the rates of electron or hole transfer across the interface, as well as the effects of surface states, surface passivation, and adsorption/desorption processes on the charge transfer kinetics and can be used to study double-layer capacitance.

2.7.8. Electrospinning unit

Electrospinning is a versatile and simple method that utilizes electrostatic repulsion between surface charges to consistently extract nanofibers from a viscoelastic fluid [66]. It has been effectively used to develop nanofibers from a wide range of materials, including polymers, ceramics, tiny molecules, and their composite, with diameters as small as tens

of nanometers. Apart from producing smooth-surfaced solid nanofibers, electrospinning has been adapted to produce nanofibers with various secondary structures, such as hollow, porous, or core-sheath-shaped ones. Usually, Electrospinning comprises four key components: a syringe pump, a spinneret, a high-voltage power source, and a collector [67,68]. When a small quantity of a viscoelastic fluid is ejected through the spinneret, it tends to appear a spherical droplet shape due to surface tension confinement. Since the droplet is connected to a sufficiently high voltage source, the body of the liquid becomes charged of the same sign. The surface tension is counteracted by the repulsion among these charges, leading to the destabilization of the spherical shape. If the repulsion is sufficiently strong to overcome the surface tension, the droplet will deform into a conical shape (Taylor cone) and finally a charged jet is ejected. At the beginning of jetting, the droplet quickly transitions into a phase commonly referred to as the "cone-jet" regime [69, 70]. Due to the combined influence of the electric field and the repulsion among surface charges, the jet keeps decreasing in diameter until it begins to bend. Next, the jet transitions into the "whipping instability" phase, where it speeds up and rapidly fluctuates in a whipping motion. Consequently, the diameter of the jet significantly reduces over time as the solvent evaporates. Eventually, the jet solidifies, yielding fibers with extremely fine diameters.

2.8. Conclusion

In this chapter, the physical properties of all the materials that have been used during experiment and synthesis procedure of all the systems is discussed. Simple electrochemical polymerization method has been employed to synthesize conducting polymer PEDOT-PSS in presence of three electrode setup by using bare ITO as a working electrode, Ag/AgCl as a reference electrode and platinum as a counter electrode. Using modified Hummer's method GO was prepared. By employing the liquid phase exfoliation (LPE) technique suggested by Coleman et al., WS₂ nanosheets were synthesized. GO/PEDOT-PSS and WS₂/PEDOT-PSS over ITO were prepared by electro-polymerization of monomer EDOT by keeping GO and WS₂ as dopants. Further, AuNPs were deposited over the surface of the GO/PEDOT-PSS/ITO and WS₂/PEDOT-PSS/ITO electrodes by performing CV in presence of a three electrode setup. Another conducting polymer, PANI has been synthesized by chemical oxidative polymerization of aniline monomer. Further, PANI-PVA composite nanofibers were prepared by utilizing facile electrospinning technique. Later, all the fabricated nanoelectrodes were functionalized with glutaraldehyde cross linking agent due to the presence of its highly reactive di aldehyde group. Then the

glutaraldehyde treated electrodes were incubated with enzyme/antibody which will be used for further sensing experiments. Next chapter deals with the physical and electrochemical properties of all the synthesized nanohybrid electrodes.

2.9. References

- [1] Rusling, J. F., and Suib, S. L. Characterizing materials with cyclic voltammetry. *Advanced Materials*, 6(12):922-930, 1994.
- [2] Sharma, A., Kumar, A., and Khan, R. A highly sensitive amperometric immunosensor probe based on gold nanoparticle functionalized poly (3, 4-ethylenedioxythiophene) doped with graphene oxide for efficient detection of aflatoxin B₁. *Synthetic Metals*, 235:136-144, 2018.
- [3] Zaaba, N. I., Foo, K. L., Hashim, U., Tan, S. J., Liu, W. W., and Voon, C. H. Synthesis of graphene oxide using modified hummers method: solvent influence. *Procedia engineering*, 184:469-477, 2017.
- [4] Weaver, C.L., Li, H., Luo, X., and Cui, X.T. A graphene oxide/conducting polymer nanocomposite for electrochemical dopamine detection: origin of improved sensitivity and specificity, *Journal of Materials Chemistry B*, 2(32):5209–5219, 2014.
- [5] Luo, X.L., Weaver, C.L., Tan, S.S., and Cui, X.T. Pure graphene oxide doped conducting polymer nanocomposite for bio-interfacing, *Journal of Materials Chemistry B*, 1(9):1340–1348, 2013.
- [6] Gligor, D., Cuibus, F., Peipmann, R., and Bund, A. Novel amperometric sensors for nitrite detection using electrodes modified with PEDOT prepared in ionic liquids. *Journal of Solid State Electrochemistry*, 21:281-290, 2017.
- [7] Sharma, A., Kumar, A., and Khan, R. A highly sensitive amperometric immunosensor probe based on gold nanoparticle functionalized poly (3, 4-ethylenedioxythiophene) doped with graphene oxide for efficient detection of aflatoxin B₁, *Synthetic Metals*, 235:136-144, 2018.
- [8] Coleman, J. N., Lotya, M., O'Neill, A., Bergin, S. D., King, P. J., Khan, U., ... and Nicolosi, V. Two-dimensional nanosheets produced by liquid exfoliation of layered materials. *Science*, 331(6017):568-571, 2011.
- [9] Baruah, S., Mohanta, D., and Betty, C. A. Composite PEDOT-PSS based highly sensitive electrochemical sensors for sensing glucose from human saliva. *Microchemical Journal*, 206:111411, 2024.

- [10] Sharma, A., Kumar, A., and Khan, R. Electrochemical immunosensor based on poly (3, 4-ethylenedioxythiophene) modified with gold nanoparticle to detect aflatoxin B₁. *Materials Science and Engineering: C*, 76:802-809, 2017.
- [11] Zhao, G., and Liu, G. Electrochemical deposition of gold nanoparticles on reduced graphene oxide by fast scan cyclic voltammetry for the sensitive determination of As (III). *Nanomaterials*, 9(1):41, 2018.
- [12] Medhi, A., Baruah, S., Singh, J., Betty, C. A., and Mohanta, D. Au nanoparticle modified GO/PEDOT-PSS based immunosensor probes for sensitive and selective detection of serum immunoglobulin g (IgG). *Applied Surface Science*, 575:151775, 2022.
- [13] Du, D. Wang, M.H., Cai, J., Qin, Y.H., and Zhang, A.D. One-step synthesis of multiwalled carbon nanotubes-gold nanocomposites for fabricating amperometric acetylcholinesterase biosensor, *Sensors and Actuators B: Chemical*, 143:524-529, 2010.
- [14] Chaudhari, S., Sharma, Y., Archana, P. S., Jose, R., Ramakrishna, S., Mhaisalkar, S., and Srinivasan, M. Electrospun polyaniline nanofibers web electrodes for supercapacitors. *Journal of Applied Polymer Science*, 129(4):1660-1668, 2013.
- [15] Wang, J., Chi, H., Zhou, A., Zheng, R., Bai, H., and Zhang, T. Facile synthesis of multi-functional elastic polyaniline/polyvinyl alcohol composite gels by a solution assembly method. *RSC advances*, 10(37):22019-22026, 2020.
- [16] Wang, Y. Preparation and application of polyaniline nanofibers: an overview. *Polymer International*, 67(6):650-669, 2018.
- [17] Subramania, A. and Devi, S. L. Polyaniline nanofibers by surfactant-assisted dilute polymerization for supercapacitor applications. *Polymers for Advanced Technologies*:19(7):725-727, 2008.
- [18] Thanpitcha, T., Sirivat, A., Jamieson, A. M., and Rujiravanit, R. Synthesis of polyaniline nanofibrils using an in situ seeding technique. *Synthetic metals*, 158(17-18):695-703, 2008.
- [19] Guan, H., Fan, L. Z., Zhang, H., and Qu, X. Polyaniline nanofibers obtained by interfacial polymerization for high-rate supercapacitors. *Electrochimica Acta*, 56(2):964-968, 2010.
- [20] Zhao, J., Qin, Z., Li, T., Li, Z., Zhou, Z., and Zhu, M. Influence of acetone on nanostructure and electrochemical properties of interfacial synthesized

- polyaniline nanofibers. *Progress in natural science: Materials International*, 25(4):316-322, 2015.
- [21] Kumar, V., Mirzaei, A., Bonyani, M., Kim, K. H., Kim, H. W., and Kim, S. S. Advances in electrospun nanofiber fabrication for polyaniline (PANI)-based chemoresistive sensors for gaseous ammonia. *TrAC Trends in Analytical Chemistry*, 129:115938, 2020.
- [22] Liu, H., Hu, X. B., Wang, J. Y., and Boughton, R. I. Structure, conductivity, and thermopower of crystalline polyaniline synthesized by the ultrasonic irradiation polymerization method. *Macromolecules*, 35(25):9414-9419, 2002.
- [23] Mirabedini, A., Foroughi, J., and Wallace, G. G. Developments in conducting polymer fibres: from established spinning methods toward advanced applications. *RSC advances*, 6(50):44687-44716, 2016.
- [24] Chaudhari, S., Sharma, Y., Archana, P. S., Jose, R., Ramakrishna, S., Mhaisalkar, S., and Srinivasan, M. Electrospun polyaniline nanofibers web electrodes for supercapacitors. *Journal of Applied Polymer Science*, 129(4):1660-1668, 2013.
- [25] Rose, A., Prasad, K. G., Sakthivel, T., Gunasekaran, V., Maiyalagan, T., and Vijayakumar, T. J. A. S. S. Electrochemical analysis of graphene oxide/polyaniline/polyvinyl alcohol composite nanofibers for supercapacitor applications. *Applied surface science*, 449:551-557, 2018.
- [26] Asiri, A. M. Electrospun polyaniline/polyvinyl alcohol/multiwalled carbon nanotubes nanofibers as promising bioanode material for biofuel cells. *Journal of Electroanalytical Chemistry*, 789:181-187, 2017.
- [27] Baruah, S., Mohanta, D., and Betty, C. A. Highly sensitive and label free on-site monitoring immunosensor for detection of Aflatoxin B₁ from real samples. *Analytical Biochemistry*, 689:115493, 2024.
- [28] Migneault, I., Dartiguenave, C., Bertrand, M. J., and Waldron, K. C. Glutaraldehyde: behavior in aqueous solution, reaction with proteins, and application to enzyme crosslinking. *Biotechniques*, 37(5):790-802, 2004.
- [29] Xiao, Z., Xie, Y., Militz, H., and Mai, C. Effect of glutaraldehyde on water related properties of solid wood, *Holzforschung*, 64:483-488, 2010.
- [30] Wan, D., Yuan, S., Li, G. L., Neoh, K. G., and Kang, E. T. Glucose biosensor from covalent immobilization of chitosan-coupled carbon nanotubes on

- polyaniline-modified gold electrode. *ACS applied materials & interfaces*, 2(11):3083-3091, 2010.
- [31] Als-Nielsen, J., Jacquemain, D., Kjaer, K., Leveiller, F., Lahav, M., and Leiserowitz, L. Principles and applications of grazing incidence X-ray and neutron scattering from ordered molecular monolayers at the air-water interface. *Physics Reports*, 246(5):251-313, 1994.
- [32] Bjork, E.M. Mesoporous Building Blocks: Synthesis and Characterization of Mesoporous Silica Particles and Films. PhD thesis, Department of Physics, Chemistry and Biology, Linkoping University Electronic Press, 2013.
- [33] Kacher, J., Landon, C., Adams, B. L., and Fullwood, D. Bragg's Law diffraction simulations for electron backscatter diffraction analysis. *Ultramicroscopy*, 109(9):1148-1156, 2009.
- [34] Yang, D., and Frindt, R. F. Powder x-ray diffraction of two-dimensional materials. *Journal of applied physics*, 79(5):2376-2385, 1996.
- [35] Costa, N., Amaral, S., Alvim, R., Nogueira, M., Schwanninger, M., and Rodrigues, J. Assessment of resin formulations and determination of the formaldehyde to urea molar ratio by near-and mid-infrared spectroscopy and multivariate data analysis. *Journal of applied polymer science*, 128(1):498-508, 2013.
- [36] Akhtar, K., Khan, S. A., Khan, S. B., and Asiri, A. M. Scanning electron microscopy: *Principle and applications in nanomaterials characterization*, pages 113-145. Springer International Publishing, 2018.
- [37] Saubermann, A. J., and Echlin, P. The preparation, examination and analysis of frozen hydrated tissue sections by scanning transmission electron microscopy and X-ray microanalysis. *Journal of Microscopy*, 105(2):155-191, 1975.
- [38] Goldstein, J. I., Newbury, D. E., Echlin, P., Joy, D. C., Fiori, C., Lifshin, E., ... and Lifshin, E. Preparation of biological samples for scanning electron microscopy. *Scanning Electron Microscopy and X-Ray Microanalysis: A Text for Biologist, Materials Scientist, and Geologists*, 495-539, 1981.
- [39] McMULLAN, D. The early development of the scanning electron microscope. In *Biological Low-Voltage Scanning Electron Microscopy*, pages 1-25. New York, NY: Springer New York, 2008.
- [40] Guerra, I., & Cardell, C. Optimizing use of the structural chemical analyser (variable pressure FESEM-EDX raman spectroscopy) on micro-size complex

- historical paintings characterization. *Journal of Microscopy*, 260(1):47-61, 2015.
- [41] Aydın, E. B., and Sezgintürk, M. K. Indium tin oxide (ITO): A promising material in biosensing technology. *TrAC Trends in Analytical Chemistry*, 97:309-315, 2017.
- [42] Bohari, N. A., Siddiquee, S., Saallah, S., Misson, M., and Arshad, S. E. Optimization and analytical behavior of electrochemical sensors based on the modification of indium tin oxide (ITO) using PANI/MWCNTs/AuNPs for mercury detection. *Sensors*, 20(22):6502, 2020.
- [43] Sophocleous, M., and Atkinson, J. K. A review of screen-printed silver/silver chloride (Ag/AgCl) reference electrodes potentially suitable for environmental potentiometric sensors. *Sensors and Actuators A: Physical*, 267:106-120, 2017.
- [44] Heinze, J. Cyclic voltammetry—"electrochemical spectroscopy". New analytical methods (25). *Angewandte Chemie International Edition in English*, 23(11), 831-847, 1984.
- [45] Ševčík, A. Oscillographic polarography with periodical triangular voltage. *Collection of Czechoslovak Chemical Communications*, 13:349-377, 1948.
- [46] Randles, J.E.B. A cathode ray polarograph. *Transactions of the Faraday Society*, 44:322-327, 1948.
- [47] Costentin, C. (2008). Electrochemical approach to the mechanistic study of proton-coupled electron transfer. *Chemical Reviews*, 108(7), 2145-2179.
- [48] Heinze, J. (1984). Cyclic voltammetry—"electrochemical spectroscopy". New analytical methods (25). *Angewandte Chemie International Edition in English*, 23(11), 831-847. 4th line 28 page
- [49] Pejčić, B., and De Marco, R. Impedance spectroscopy: Over 35 years of electrochemical sensor optimization. *Electrochimica acta*, 51(28):6217-6229, 2006.
- [50] Formisano, N. A study on the optimisation of electrochemical impedance spectroscopy biosensors. PhD Thesis, University of Bath, 2015.
- [51] Qu, D., Ji, W. and Qu, H. Probing process kinetics in batteries with electrochemical impedance spectroscopy. *Communications Materials* 3:61, 2022.

- [52] Delcourt-Lancon, A. Electrochemical analysis supported by macro and microelectrode array. PhD thesis, Department of Chemistry, Durham University, 2011.
- [53] Mansor, N.B. Development of catalysts and catalyst supports for polymer electrolyte fuel cells. PhD thesis, Department of Chemical Engineering, University College London, 2015.
- [54] Cesiulis, H., Tsyntsaru, N., Ramanavicius, A. and Ragoisha, G. The study of thin films by electrochemical impedance spectroscopy. In *Nanostructures and thin films for multifunctional applications*, pages 3-42, ISBN:978-3-319-30197-6. Springer, Cham, 2016.
- [55] Macdonald, J.R. and Barsoukov, E. Impedance spectroscopy: theory, experiment, and applications. John Wiley & Sons, 2018.
- [56] Chang, B.Y. and Park, S.M. Electrochemical impedance spectroscopy. *Annual Review of Analytical Chemistry*, 3(1):207-229, 2010.
- [57] Randles, J.E.B. Kinetics of rapid electrode reactions. *Discussions of the faraday society*, 1:11-19, 1947.
- [58] Scholz, F. Electroanalytical methods. Springer, Berlin, 2nd edition, 2010.
- [59] Bard, A.J., Faulkner, L.R. and White, H.S. Electrochemical methods: fundamentals and applications. John Wiley & Sons, 2nd edition, 2000.
- [60] Roach, K. L. Electrochemical models for electrode behavior in retinal prostheses. PhD thesis, Massachusetts Institute of Technology, 2003.
- [61] Park, S.M., and Yoo, J.S. Electrochemical impedance spectroscopy for better electrochemical measurements. *Analytical Chemistry*, 75:A455–81, 2003.
- [62] Rama, K., Shweta, D., and Jasmin, K. Electrode disorder, electrochemical processes and governing length scales. *Journal of the Indian Institute of Science*, 96(4):365-382, 2016.
- [63] Qu, D., Wang, G., Kafle, J., Harris, J., Crain, L., Jin, Z., and Zheng, D. Electrochemical impedance and its applications in energy-storage systems. *Small Methods*, 2(8):1700342, 2018.
- [64] Rezaei, B. and Irannejad, N. Electrochemical detection techniques in biosensor applications. In *Electrochemical biosensors*, pages 11-43, ISBN:9780128164914. Elsevier, 2019.

- [65] Lane, R. F., and Hubbard, A. T. Differential double pulse voltammetry at chemically modified platinum electrodes for in vivo determination of catechol amines. *Analytical Chemistry*, 48(9):1287-1293, 1976.
- [66] Xue, J., Wu, T., Dai, Y., and Xia, Y. Electrospinning and electrospun nanofibers: Methods, materials, and applications. *Chemical reviews*, 119(8):5298-5415, 2019.
- [67] Li, Y., Zhu, J., Cheng, H., Li, G., Cho, H., Jiang, M., ... and Zhang, X. Developments of advanced electrospinning techniques: A critical review. *Advanced Materials Technologies*, 6(11):2100410, 2021.
- [68] Barhoum, A., Pal, K., Rahier, H., Uludag, H., Kim, I. S., and Bechelany, M. Nanofibers as new-generation materials: From spinning and nano-spinning fabrication techniques to emerging applications. *Applied Materials Today*, 17:1-35, 2019.
- [69] Shin, D., Kim, J., Choi, S., Lee, Y. B., and Chang, J. Droplet-jet mode near-field electrospinning for controlled helix patterns with sub-10 μm coiling diameter. *Journal of Micromechanics and Microengineering*, 29(4):045004, 2019.
- [70] Joy, N., Anuraj, R., Viravalli, A., Dixit, H. N., and Samavedi, S. Coupling between voltage and tip-to-collector distance in polymer electrospinning: Insights from analysis of regimes, transitions and cone/jet features. *Chemical Engineering Science*, 230:116200, 2021.